Materials Research Bulletin 193 (2026) 113653

Contents lists available at ScienceDirect

Materials Research Bulletin

journal homepage: www.elsevier.com/locate/matresbu

Research Papers

Plasma transferred arc intergranular and transgranular orientation processing route for enhanced nickel-matrix coating corrosion and wear resistance

Augustine Nana Sekyi Appiah [a,*], Przemysław Snopiński [b], Marek Pagáč [c], Yao Mawuena Tsekpo [b], Benjamin Agyei-Tuffour [d], Gilmar F. Batalha [e], Marcin Adamiak [a]

[a] Materials Research Laboratory, Faculty of Mechanical Engineering, Silesian University of Technology, 18A Konarskiego Street, 44-100 Gliwice, Poland
[b] Department of Engineering Materials and Biomaterials, Faculty of Mechanical Engineering, Silesian University of Technology, 18A Konarskiego Street, 44-100 Gliwice, Poland
[c] Center of 3D Printing Protolab, Department of Machining, Assembly and Engineering Technology, Faculty of Mechanical Engineering, VSB-TU Ostrava, 17. listopadu 2172/15, 708 00 Ostrava-Poruba, Czech Republic
[d] Department of Materials Science and Engineering, University of Ghana, Accra, Ghana
[e] Department of Mechatronics and Mechanical Systems Engineering, Polytechnic School of Engineering of the University of Sao Paulo (USP), São Paulo 05508-900, Brazil

ARTICLE INFO

Keywords:
Grain boundary
FCC texture
Electron backscatter diffraction (EBSD)
Geometrically necessary dislocation (GND)

ABSTRACT

This study introduces a novel Plasma Transferred Arc Welding (PTAW) processing route for depositing high-performance NiCrBSi coatings on structural steel. The innovation of this work lies in the strategic use of a low standoff distance (5 mm) in combination with low arc currents (60 A and 70 A) to tailor the coating's microstructure for superior wear and corrosion resistance, addressing a significant challenge in extending the lifespan of machine tools. The coating prepared at 60 A (C60A) demonstrated a significant improvement in properties compared to the one prepared at 70 A (C70A). Quantitatively, the C60A coating achieved a maximum microhardness of 754.0 $HV_{0.5}$, a 26.8 % reduction in corrosion current density, and a 38 % lower wear rate ($p < 0.01$). These enhancements are attributed to a more refined microstructure, a higher volume fraction of beneficial FCC texture components, and a lower density of geometrically necessary dislocations (1.04×10^{13} m^{-2} for C60A vs. 1.08×10^{13} m^{-2} for C70A). This research provides a viable pathway for fabricating durable and reliable Ni-based coatings for demanding industrial applications.

1. Introduction

The global push for sustainable development and responsible production and consumption practices has put a spotlight on the need to extend the lifespan of industrial machinery and components [1,2]. Machine tools, which are fundamental to numerous industries, are often subjected to harsh operating conditions, leading to degradation through wear and corrosion. This premature failure not only results in significant economic losses due to downtime and replacement costs but also has a considerable environmental impact stemming from the consumption of non-regenerative resources and the generation of industrial waste [3–6]. Therefore, there is a need for advanced surface engineering solutions that can enhance the durability and performance of these critical components.

Surface engineering techniques, such as thermal spraying [7], laser cladding [8], and Plasma Transferred Arc Welding (PTAW) [9], are widely employed to deposit protective coatings on industrial components. Among these, PTAW is a versatile and cost-effective method that can produce thick, dense, and metallurgically bonded coatings [10]. NiCrBSi alloys are a popular choice for these coatings due to their excellent intrinsic resistance to wear and corrosion [11].

Previous research on PTAW-deposited NiCrBSi coatings has explored various strategies to optimize their properties, primarily through the optimization of processing parameters like travel speed [12], gas flow rate [13], and current [14]. Many studies have focused on using high PTA currents (100 – 500 A) to ensure complete melting of the powder and achieve good bonding [13,15,16]. However, high currents can lead to issues such as excessive dilution, a large heat-affected zone, and

---

* Corresponding author.
E-mail address: augustine.appiah@polsl.pl (A.N.S. Appiah).

https://doi.org/10.1016/j.materresbull.2025.113653
Received 10 February 2025; Received in revised form 11 June 2025; Accepted 5 July 2025

premature electrode degradation [17]. More recent studies have investigated the use of lower currents (<100 A), but the results have been inconsistent, with some reporting problems like incomplete fusion and poor coating quality. Ikpe et al. [17] investigated current intensities of 50 A, 100 A, 150 A, and 190 A, noting that the lowest current of 50 A resulted in arc instability and incomplete fusion. Goa et al. [18] explored the influence of lower PTA currents ranging from 50 A to 65 A, and reported suboptimal hardness and tribological properties. It is noteworthy however, that a common practice in these studies has been the use of a relatively large standoff distance (8–20 mm) to avoid overheating the substrate [9,19,20],.

This study addresses the existing gap in the literature by investigating a novel PTAW processing route that combines a low standoff distance of 5 mm with low arc currents – 60 A and 70 A. The central hypothesis is that this unique combination of parameters can overcome the challenges associated with low-current PTAW, such as poor corrosion and wear resistance, leading to the fabrication of high-quality, high-performance NiCrBSi coatings. The significance of this work is twofold, catering to both scientific and industrial significance. Scientifically, it provides a detailed, mechanism-based understanding of how low-current PTAW processing influences the microstructural evolution, including grain size, grain boundary characteristics, dislocation density, and texture and, consequently, the corrosion and tribological performance of NiCrBSi coatings. Industrially, this research offers a practical and cost-effective method for producing highly durable coatings for machine tools and other components used in demanding sectors like mining, transport, and petroleum. By enhancing the service life of these components, this work contributes to more sustainable manufacturing practices, reducing resource consumption and waste generation.

2. Materials and methods

2.1. Materials

The NiCrBSi powders utilized for sample fabrication were procured commercially as gas atomized powders (Durmat 456). These powders exhibit a spherical morphology, as depicted in Fig. 1**A**, with an observed uneven surface texture (Fig. 1**B**). Characterization of the powders revealed a particle size of 126 μm (d_{90}) and a calculated dimensionless factor of uniformity (span) of 2.1, indicating a notable degree of particle non-uniformity [21], as illustrated by the size frequency distribution plot in Fig. 1**C**. The chemical composition analysis of the powder was conducted using energy dispersive X-ray spectroscopy (EDS), with five (5) random powder particles subjected to EDS point analyses, and the resulting average composition depicted in Fig. 1**D**

Prior to coating deposition, X-ray diffraction (XRD) analysis was performed on the powders, with Fig. 1**E** showing the outcomes. The identified phases predominantly included γ-Ni (ICSD No. 260,169), $Cr_{23}C_6$ (ICSD No. 617,488), Cr_3C_2 (ICSD No. 181,711), alongside minor intensity peaks corresponding to $Ni_{31}Si_{12}$ (ICSD No. 9106) and Ni_3B (ICSD No. 75,794). It's noteworthy that certain peaks corresponding to different phases were observed to overlap with others. For example, at $2\theta \sim 52^\circ$, a high-intensity peak corresponding to the (111) γ-Ni phase overlapped with relatively lower intensity peaks attributed to the (006) $Ni_{31}Si_{12}$ and (102) Ni_3B phases. All identified overlaps are comprehensively presented in Fig. 1**E**.

The base material used in this study was a 15HM low alloy steel, possessing a hardness of 153 ± 5.0 $HV_{0.5}$. Its chemical composition, determined through EDS analysis, is depicted in Fig. 1**F**.

2.2. Coaxial powder-feeding plasma transferred arc welding process

The powder plasma transferred arc welding (PPTAW) system employed in this study is the Castolin Eutectic GAP 2001 DC machine, configured to facilitate directed energy deposition (DED) for coating preparation. The plasma torch, positioned coaxially, executes the coating process as illustrated in Fig. 2. The plasma arc control unit is fitted with a reservoir containing Argon 5.0 gas, ensuring 99.99 % purity in accordance with ISO 14,175-I1:2009 standards. A gas mixture comprising 5 % hydrogen (H_2) and argon (Ar) following ISO 14,175-R1-ArH-5 welding mixture guidelines serves as the shielding and carrier gas. Process parameters for PPTAW include a 4 mm electrode diameter,

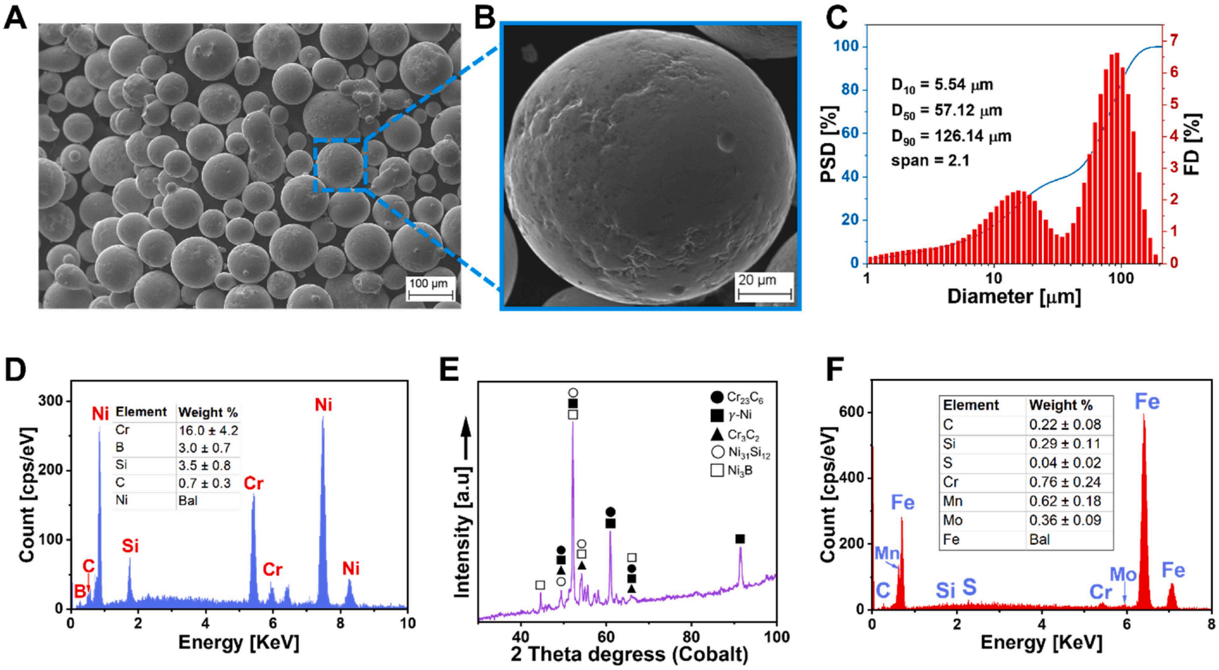

Element	Weight %
Cr	16.0 ± 4.2
B	3.0 ± 0.7
Si	3.5 ± 0.8
C	0.7 ± 0.3
Ni	Bal

Element	Weight %
C	0.22 ± 0.08
Si	0.29 ± 0.11
S	0.04 ± 0.02
Cr	0.76 ± 0.24
Mn	0.62 ± 0.18
Mo	0.36 ± 0.09
Fe	Bal

Fig. 1. **A.** SEM image of NiCrBSi powder particles, **B.** Morphology of gas atomized NiCrBSi powder particle showing an uneven spherical surface, **C.** Plot of particle size distribution (PSD) and frequency distribution (FD) as functions of particle diameter, **D.** Chemical composition of NiCrBSi powder obtained from energy dispersive x-ray spectroscopy (EDS), **E.** X-ray diffraction (XRD) phase analysis of NiCrBSi powder, and **F.** Chemical composition of base material 15HM steel obtained from EDS analysis.

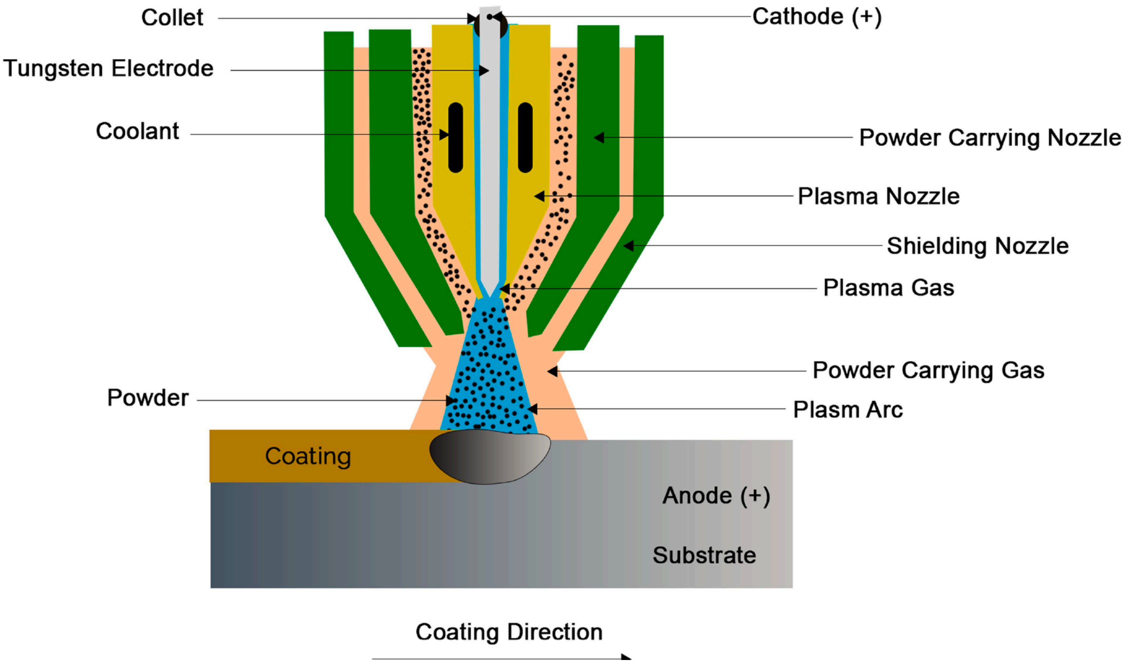

Fig. 2. Schematic diagram of coaxial powder-feeding plasma transferred arc welding process.

2 mm plasma nozzle size, plasma gas flow rate of 2.0 L/min, travel speed set at 2.0 mm/s, and a thermal coefficient of 0.6. For the novelty of this study, the standoff distance was maintained at 5 mm while preparing coatings using low plasma transferred arc (PTA) currents. Two distinct specimen categories were fabricated for analyses: the first, designated as C70A, was prepared with a PTA current of 70 A, while the second, denoted as C60A, was prepared with a PTA current of 60 A. These designations will be consistently referenced throughout this paper.

2.3. *Characterization*

Metallographic samples designated for analysis underwent a preparation regimen which involved 500, 800, 1200, and 2000-grit SiC sheet grinding followed by diamond suspensions 9 µm, 6 µm, 3 µm, 1 µm, and final polishing to achieve a mirror finish utilizing 0.04 µm colloidal silica. For microstructural characterization, both Zeiss LOM (with Nomarski differential interference microscopy capability) and SEM instruments equipped with an EDS system (EVO 15 MA) were employed. Electron Backscatter Diffraction (EBSD) was utilized to perform grain size and crystallographic analyses, with a step size set to 0.2 µm at a voltage of 20 kV.

X-ray diffraction (XRD) analysis was conducted using the PANalytical X'Pert Pro diffraction system (Panalytical B.V. The Netherlands). A cobalt anode lamp (KαCo $\lambda = 0.179$ nm) was utilized, operating at a voltage of 40 kV with a filament current intensity of 30 mA. The measurements were executed in the Bragg–Brentano geometry over an angular range of 30 – 100° 2θ, employing a step size of 0.05° and a step count time of 100 s. The resultant diffractograms underwent comprehensive analysis using the X'Pert High Score Plus software (version 3.0e), in conjunction with the dedicated Inorganic Crystal Structure Database-ICSD from FIZ, Karlsruhe, Germany.

2.4. *Corrosion investigations*

The corrosion resistance investigations involved potentiodynamic testing, employing an Atlas 0531 EU potentiostat in conjunction with a standard three-electrode system immersed in a 3.5 % NaCl aqueous solution at room temperature. The auxiliary electrode utilized was a platinum-based PtP-201 electrode, while an Ag/AgCl electrode served as the reference electrode. Following a stabilization period of 3600 s to achieve an open circuit potential (E_{ocp}), corrosion testing commenced. Anodic polarization curves were then generated employing a scan rate of 0.375 mV s^{-1}, with the potential measured using Eq. (1):

$$E_{start} = E_{ocp} - 100\ mV \tag{1}$$

The slow scan rate of 0.375 mVs^{-1} was chosen to ensure the system remains in a quasi-steady state, thus minimizing measurement artifacts. The tests terminated upon reaching a 2 V potential (E_{final}), after which polarity reversal facilitated the recording of curves returning to E_{start}. Using the Tafel approach, parameters including polarization resistance (R_{pol}), corrosion current density (i_{corr}) and corrosion potential (E_{corr}) were estimated with the aid of AtlasLab software. Electrochemical impedance spectroscopy (EIS) experiments were conducted using the same potentiostat setup, with the NaCl aqueous solution maintained at the free potential. The signal amplitude was set at 10 mV, covering a frequency range of 100 kHz to 10 mHz. This frequency range for EIS has served as a standard range used for studying corrosion phenomena in several coatings [22–24], allowing for the characterization of both high-frequency (charge transfer) and low-frequency (diffusion) processes.

2.5. *Tribological assessment*

The metallographic cross-sectional Vickers hardness of the specimens was evaluated using the FM-ARS 9000 hardness tester (Future Tech Corporation, Tokyo, Japan) with a 4.9 N load. Microhardness measurements were conducted on XY cross-sections of the samples directly after metallographic polishing. The hardness assessment covered three regions in each specimen's cross-section namely the coating middle zone, interface, and substrate. For each section, there were 64 measurements, covering a 1.4 mm × 1.4 mm area, arranged in an 8 × 8 matrix pattern with a consistent horizontal and vertical displacement of 0.20 mm between each measurement.

Wear resistance experiments were conducted using the CSM tribometer (CSM Instruments, Switzerland) employing the ball-on-plate method in a dry sliding environment. A zirconium oxide (ZrO_2) G28 ball with a diameter of 6 mm and a marked minimum hardness of 940 HV, served as the opposing specimen. The maximum contact pressure was determined using Hertzian contact theory, as expressed by Eq. (2), with contact radius calculated according to Eq. (3).

$$P_{max} = \frac{3F}{2\pi a^2} \tag{2}$$

$$a = \sqrt[3]{\frac{\frac{3F}{8}\cdot\left(\frac{1-\vartheta_2^2}{E_1}\right) + \left(\frac{1-\vartheta_2^2}{E_2}\right)}{\frac{1}{d_1}+\frac{1}{d_2}}} \tag{3}$$

Where: P_{max} is maximum contact pressure (GPa), F is normal load (N), a is contact radius (mm), ϑ is Poisson's ratio, E is Young's modulus (GPa), d is diameter of curvature (mm), and designations $_1$ – tested samples and $_2$ – counter samples ball. The Young's modulus and Poisson's ratio of NiCrBSi were obtained from literature [25,26]. The wear test was conducted with a normal load of 30 N and a test distance of 100 m, maintaining a frequency of 2.0 Hz for all specimens.

The wear rate (Q) was calculated using Eq. (4), where the sliding distance (L_s) in m, and volume loss (V_s) in m^3 were accounted for.

$$Q = \frac{V_s}{L_s} \tag{4}$$

According to Archard's Law, the hardness is inversely proportional to the volume. This theory, expressed in Eq. (5), was used to relate volume loss to hardness, considering the load, wear coefficient, and hardness.

$$V_s = \frac{kWL_s}{H} \tag{5}$$

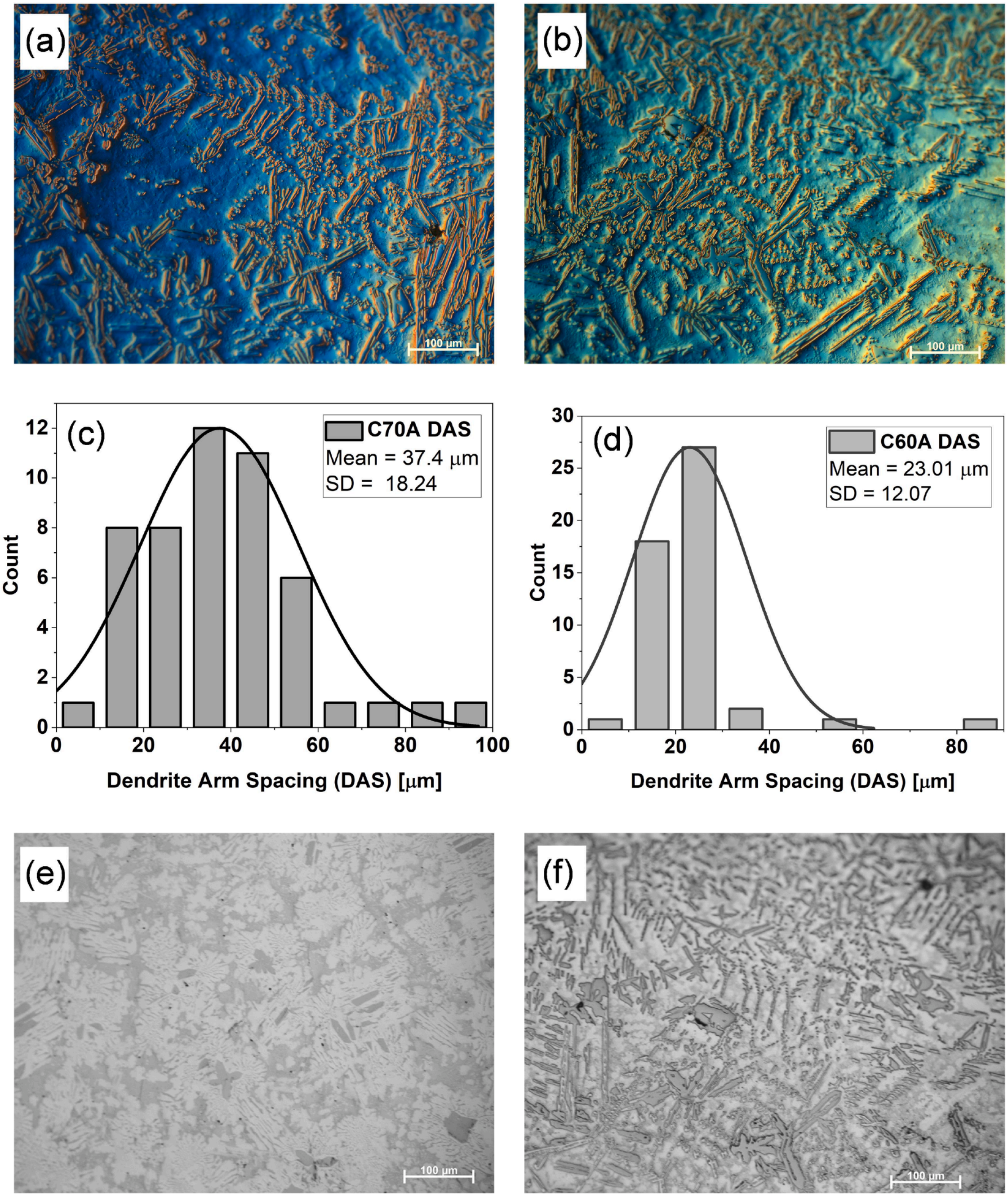

Fig. 3. **(a)** Nomarski micrograph of C70A coating MZ, **(b)** Nomarski micrograph of C60A coating MZ, **(c)** DAS of C70A coating, **(d)** DAS of C60A coating, **(e)** bright-field optical micrograph of C70A MZ, and **(f)** bright-field optical micrograph of C60A MZ.

Where W is the load, k is the wear coefficient and H is the hardness. The tests were performed under atmospheric conditions with a relative humidity of 50 – 60 % at ambient temperature. Coefficient of friction (COF) values were determined based on the conducted measurements. Prior to testing, samples and counter samples were cleaned using ethanol.

2.6. Statistical analysis

Statistical analysis was performed to determine the significance of the differences between the C70A and C60A coatings. A two-sample Student's *t*-test assuming unequal variances was used. A p-value of less than 0.05 was considered statistically significant.

3. Results

3.1. Microstructure

The microstructural analyses of the middle zone (MZ) of C70A and C60A coatings, conducted using Nomarski microscopy, are depicted in Figs. 3**(a)** and **3(b)** respectively. The differential interference contrast revealed distinct dendritic microstructures with intergranular eutectics in both specimens. Notably, the dendrite arm spacing (DAS) in the C70A middle zone exhibited an average of approximately 37 µm (Fig. 3**(c)**), surpassing the average DAS of approximately 23 µm observed in the C60A middle zone (Fig. 3**(d)**). DAS is linked to the cooling rate during solidification, with higher values indicating slower cooling rates [27]. Consequently, the C70A coating, formed with a 70 A PTA current, experienced a slower cooling rate compared to its counterpart prepared with 60 A current, leading to a less defined dendritic structure under bright field optical microscopy (Fig. 3**(e)**). In contrast, the C60A coating displayed well-defined dendrites (Fig. 3**(f)**), reminiscent of those observed with Nomarski microscopy. To elucidate the structure and composition of the dendritic structures formed, an in-depth analysis of the middle zones was conducted with scanning electron microscopy (SEM) coupled with energy dispersive X-ray spectroscopy (EDS).

Fig. 4**(a)** illustrates SEM images of the MZ of the C70A coating alongside chemical composition distribution maps. Correspondingly, Fig. 4**(b)** presents SEM images and chemical composition distribution maps for the C60A coating. These images reveal dendrites predominantly comprising Cr-rich phases nucleated within the Nickel matrix upon solidification. EDS mapping indicates a notable affinity of Si and Fe to the Nickel matrix. The presence of Fe in the MZ of the coatings is traced back to its origin from the 15HM steel substrate. Conversely, C is detected in relatively lower quantities in the coating MZ, primarily due to the diffusion of Fe and C across the coating-substrate interface during the coating process. Carbon exhibits a stronger association with Cr-rich dendritic sites in the coating prepared with a 60 A current compared to a 70 A current. This suggests a more pronounced formation of chromium carbide compounds in the coating produced with lower PTA current [28].

At the interface, both specimens exhibit a coarse-grained heat-affected zone (CGHAZ). The most notable distinction between the interfaces of the examined specimens occurs at the transition zone (TZ). Moving from the interface into the MZ, the TZ of the C70A coating (Fig. 5**(a)**) shows a progression of solidification modes: from cellular dendritic growth solidification (CDGS), through planar growth solidification (PGS), and ending with dendritic growth solidification (DGS) [11]. In contrast, the C60A coating (Fig. 5**(b)**) exhibits solidification modes starting with PGS and terminating with DGS. The presence of CDGS in the TZ of the C70A coating facilitates the nucleation of interfacial precipitates (I_{PR}) at the TZ, a phenomenon not observed in the TZ of the C60A coating. The CDGS originates from grain growth competition owing to the higher heat retention in the C70A coating, causing slower cooling rates [29]. The growth of grains with relatively lower growth rates are interrupted by those having higher growth rates, resulting in the oriented microstructure with numerous precipitates. The precipitates appear to be continuous and fine, indicating good weldability [30].

Elemental analysis using EDS maps reveals dominant segregation of Cr and Ni within the coating, while Si and B are observed to diffuse into the substrate material from the coating. Similarly, Fe and C are observed to diffuse across the interface into the coating MZ. However, the diffusion of Si and B from the coating into the substrate, as well as the diffusion of Fe and C from the substrate into the coating, is not as pronounced as typically seen in mechanical coating/substrate bonding

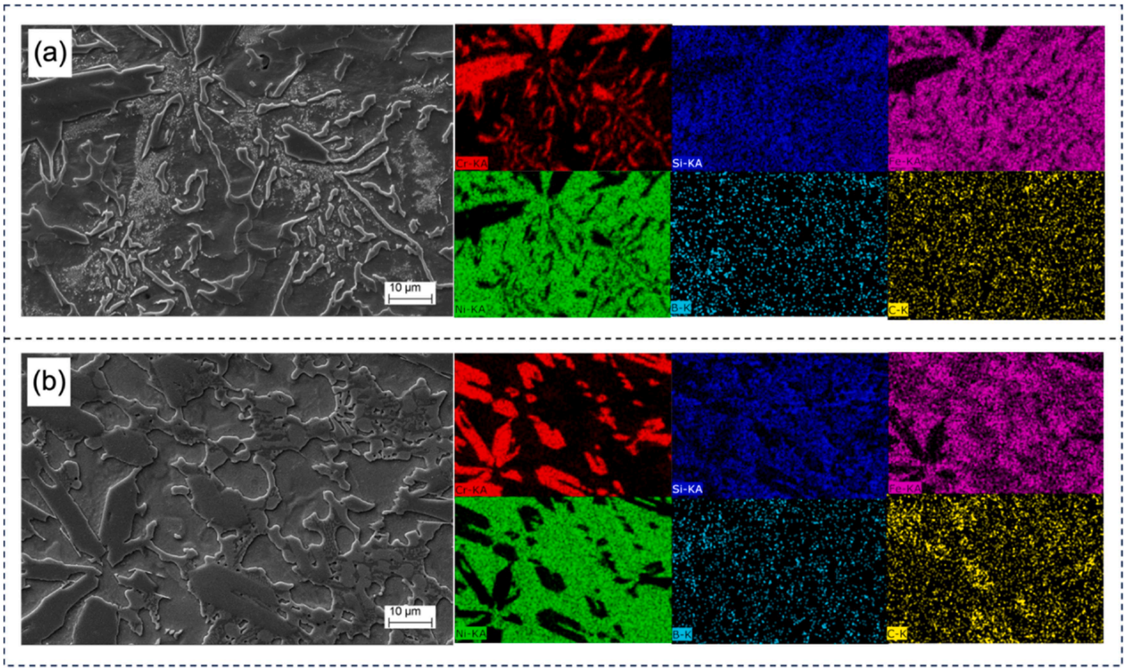

Fig. 4. SEM images of coating microstructure and structural chemical composition maps from energy dispersive X-ray spectroscopy (EDS) (a) middle zone (MZ) of C70A coating **(b)** MZ of C60A coating.

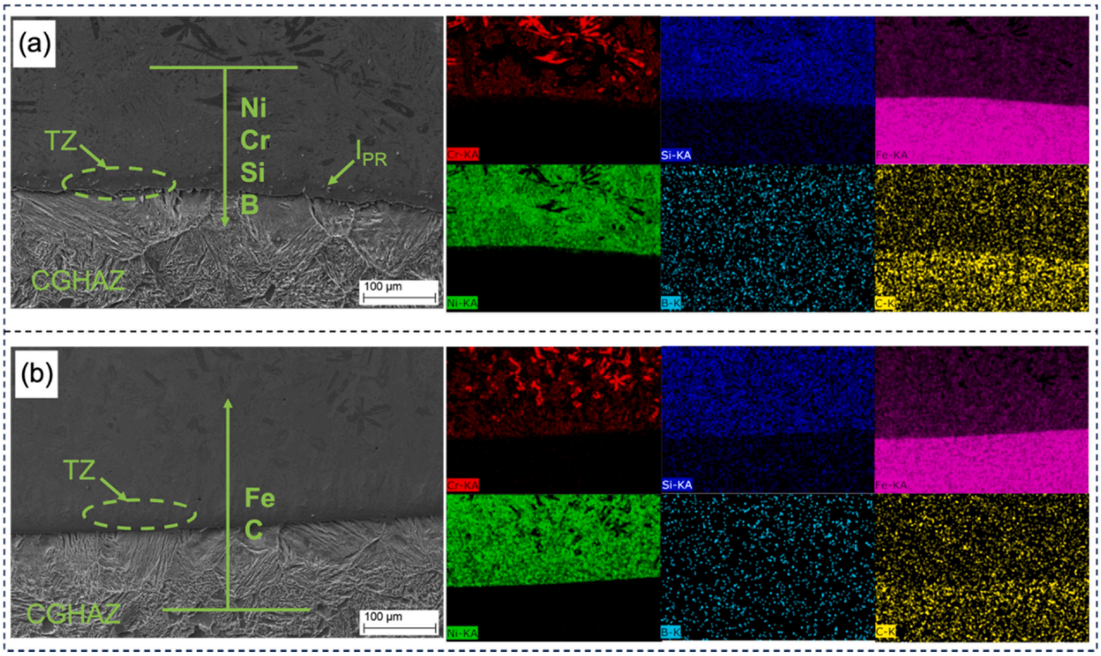

Fig. 5. SEM images of the coating – substrate interfaces with EDS chemical composition maps showing the interfacial chemical distribution and diffusion (a) interface of C70A, and **(b)** interface of C60A.

[31]. This indicates that both coatings C70A and C60A are metallurgically bonded to the substrate material through a diffusion layer [32].

3.1.1. *Phase evolution*

Fig. 6 shows X-ray diffraction (XRD) spectra of the prepared coatings, displaying characteristic peaks corresponding to face-centered cubic (FCC) structured Nickel (γ-Ni) a = b = c = 3.528 Å), FCC $Cr_{23}C_6$ (a = b = c = 10.630 Å), and orthorhombic Cr_3C_2 (a = 5.485 Å, b = 2.789 Å, c = 11.474 Å) phases. In comparison to the XRD analysis of the powder prior to coating application (Fig. 1E), the absence of $Ni_{31}Si_{12}$ and Ni_3B phases was notable following the coating deposition process. This observation aligns with findings from previous studies, such as those by Deenadayalan et al. [33] and Chen et al. [34]. These studies indicate a parallel occurrence where, upon the deposition of NiCrBSi powders via the PTA method, the concentration of the precipitated Nickel silicide phase fell below the XRD detection limit, corroborating our current observations.

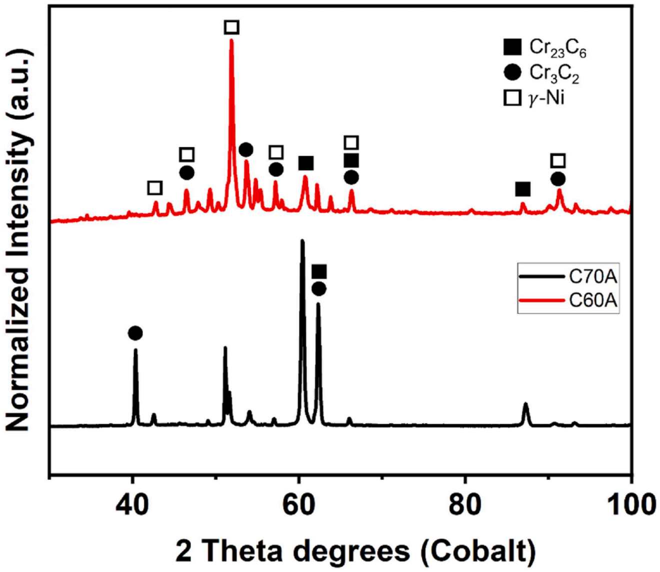

Fig. 6. X-ray diffraction (XRD) spectra of the coatings C70A and C60A.

Common peaks are observed in both coatings, with varying intensities. The (111) γ-Ni phase dominates, exhibiting a broader peak with higher intensity in the C60A coating at 2θ ~ 52° Similarly, at 2θ ~ 61°, a peak is observed representing an overlap of (002) γ-Ni and (131) $Cr_{23}C_6$ phases. Notably, at 2θ ~ 60°, the coating prepared at 70 A retains the (006) $Cr_{23}C_6$ phase more prominently compared to the 60 A current. Moreover, at 2θ ~ 62°, the overlapping peak of $Cr_{23}C_6$ and Cr_3C_2 phases is broader and more intense at 70 A current than at 60 A. However, all three phases γ-Ni, $Cr_{23}C_6$, and Cr_3C_2 overlap at 2θ ~ 64°, with a more pronounced peak in the coating prepared with 60 A. Additionally, exclusive peaks at 2θ ~ 46°, 57°, and 91°, all attributed to the γ-Ni phase, are observed only in the coating prepared with 60 A current, indicating its dominance as the strengthening phase. The greater number of peaks in the XRD spectra at 60 A compared to 70 A is attributed to the slower cooling rate at 70 A, reducing the rate of dissolution of phases into the solid solution.

Despite the presence of Fe in the coatings' microstructure confirmed by EDS analysis, no discernible Fe-based compounds or phases were detected in the XRD analyses, consistent with prior literature [35–37],. It is worth noting that some researchers suggest the γ-Ni phase may incorporate minor amounts of Si and Fe within its solid solution [38,39]. The strength of plasma sprayed coatings are often dependent on the evolved or precipitated phases upon coating solidification. The grain size, grain orientation and even the texture contribute significantly to the overall performance of the coating [11]. In this regard, a deeper examination of the XRD-identified phases was undertaken using electron backscatter diffraction (EBSD).

3.1.2. *Grains size and orientation*

Fig. 7**(a)** displays the grain orientation map for the C70A coating and Fig. 7**(b)** shows the same for the C60A coating. The inverse pole figures (IPF) show Nickel (γ-Ni) and $Cr_{23}C_6$ phases having crystal orientations of [111],[001], and [101], characteristic of the face-centered cubic (FCC) crystal structure. The Cr_3C_2 phase however is identified by an orthorhombic structure having a crystal orientation of [010],[001], and [100]. On the grain orientation maps, the high-angle grain boundaries (HAGBs), having misorientation angles greater than 15° are represented

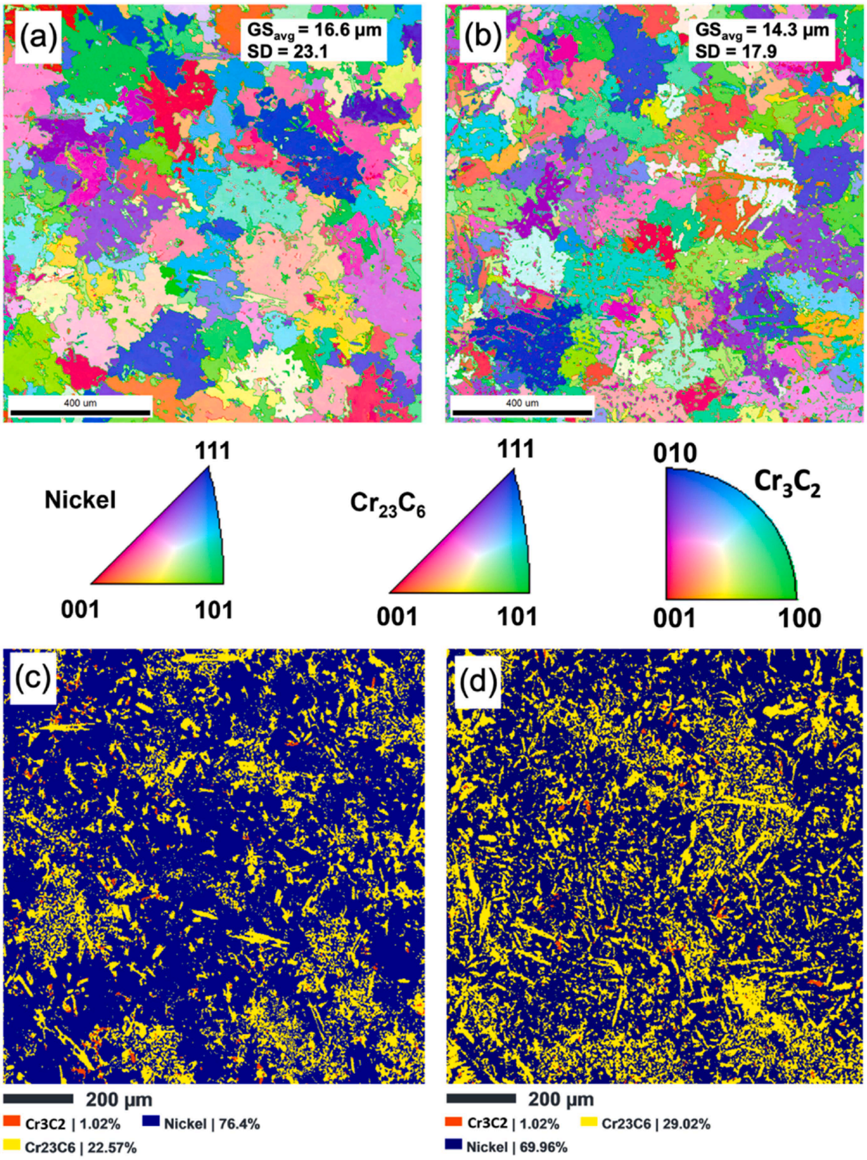

Fig. 7. Electron backscatter diffraction (EBSD) inverse pole figure (IPF), grain and phase maps (a) Grain orientation map of C70A coating showing the average grain size, **(b)** grain orientation map of C60A coating showing the average grain size, **(c)** phase distribution map of C70A coating, and **(d)** phase distribution map of C60A coating.

by green lines. Low-angle grain boundaries (LAGBs) having misorientation angles between 2° and 15° are represented by red lines. The most notable distinction between the examined coatings are the grain sizes. The coating prepared with 70 A current exhibits an all-phase inclusive average grain size of approximately 16.6 µm (grain tolerance angle, GTA = 2°). For individual phases, the γ-Ni phase had an average grain size of approximately 23.7 µm (GTA = 2°), the $Cr_{23}C_6$ phase had an average grain size of approximately 6.4 µm (GTA = 2°), and the Cr_3C_2 phase had an average grain size of approximately 3.7 µm (GTA = 2°).

On the other hand, a noteworthy grain refinement was evident in the coating prepared with a lower PTA current of 60 A. This coating had an all-phase inclusive average grain size of approximately 14.3 µm (GTA = 2°). The average grain size of the γ-Ni phase in this coating was approximately 20.9 µm (GTA = 2°). The $Cr_{23}C_6$ phase in this coating recorded an average grain size of approximately 5.2 µm (GTA = 2°), and the Cr_3C_2 phase had an average grain size of approximately 2.2 µm (GTA = 2°).

Quantitative analysis of the phases was carried out via EBSD phase composition analyses. The phase map of the C70A coating is shown in Fig. 7**(c)**. The image shows a predominant γ-Ni phase constituting approximately 76.4 % of the examined area. The $Cr_{23}C_6$ phase followed with a composition of 22.6 % and the Cr_3C_2 phase was the least, at 1.02 %. A similar trend was observed from the phase analysis of the C60A coating (Fig. 7**(d)**). The γ-Ni phase dominated with approximately 67 %, followed by the $Cr_{23}C_6$ phase at 29.02 %, and the Cr_3C_2 phase had the least composition at 1.02 %. Thus, the dominant FCC γ-Ni and $Cr_{23}C_6$ phases were identified as pivotal contributors to the bulk properties of the coatings. Consequently, in-depth microstructural investigations were focused on these phases.

3.1.3. Grain boundary character distribution (GBCD)

The interconnectivity and energetic properties of grain boundaries are essential contributors to the performance of NiCrBSi coatings [40]. GBCD is the proportional length of grain boundaries for a given misorientation, responsible for the material's behavior towards conditions such as creep and fatigue, as well as reducing corrosion resistance and intercrystalline crack propagation [41]. GBCD comprehensively emphasizes the concentration and characteristics of LAGBs, HAGBs, and coincidence site lattice (Σ-CSL) boundaries. Fig. 8**(a)** presents a comparative analysis of the volume fractions of LAGBs, HAGBs, and Σ-CSL boundaries in the Nickel phase. The investigation reveals that the C60A coating exhibits a higher volume fraction of LAGBs, amounting to 0.29, compared to the C70A coating, with a fraction of 0.18. The C70A coating demonstrates a greater volume fraction of HAGBs, reaching 0.68, in contrast to the C60A coating. Moreover, Σ-CSL boundaries exhibit the lowest volume fractions for this phase in both coatings. Conversely, in the $Cr_{23}C_6$ phase (Fig. 8**(b)**), LAGBs display the lowest volume fraction, approximately 0.19, in both coatings. HAGBs, on the other hand, showcase the highest volume fractions, with the C60A coating surpassing the C70A coating. Additionally, CSL boundaries in this phase exhibit volume fractions higher than LAGBs but lower than HAGBs, with the C70A coating showing a higher number of CSL boundaries.

The volumetric composition of HAGBs and LAGBs within the γ-Ni phase of C70A and C60A coatings, as depicted in Supplementary **Fig. S1 (a)** and **S1(b)** respectively, reveals distinct proportions. In the C70A coating, HAGBs constitute 83.5 % of the γ-Ni phase volume, with LAGBs comprising the remaining 17.5 %. Similarly, in the C60A coating, HAGBs dominate, constituting 75.4 % of the γ-Ni phase volume, while LAGBs occupy 24.6 %. This dominance of HAGBs is consistent across phases, including $Cr_{23}C_6$. In both the C70A and C60A coatings, the $Cr_{23}C_6$ phase exhibits a significant proportion of HAGBs, with respective volumes of 87 % (**Fig. S1(c)**) and 86.7 % (**Fig. S1(d)**), accompanied by LAGBs at 13 % and 13.3 %. The prevalence of HAGBs suggests elevated interfacial energies within the coatings, impeding dislocation motion and consequently enhancing their stability and strength [42]. The observed augmentation in the volume fraction of LAGBs with the reduction of current to 60 A implies enhanced intergranular corrosion resistance within the C60A coating compared to its C70A counterpart. This phenomenon can be attributed to the intrinsic low-energy characteristics inherent in LAGBs, underscoring the superior protective attributes of the C60A coating against intergranular corrosion [43].

The coincidence site lattice (Σ-CSL) concept pertains to the reciprocal density of coincident atomic sites within adjacent grain lattices,

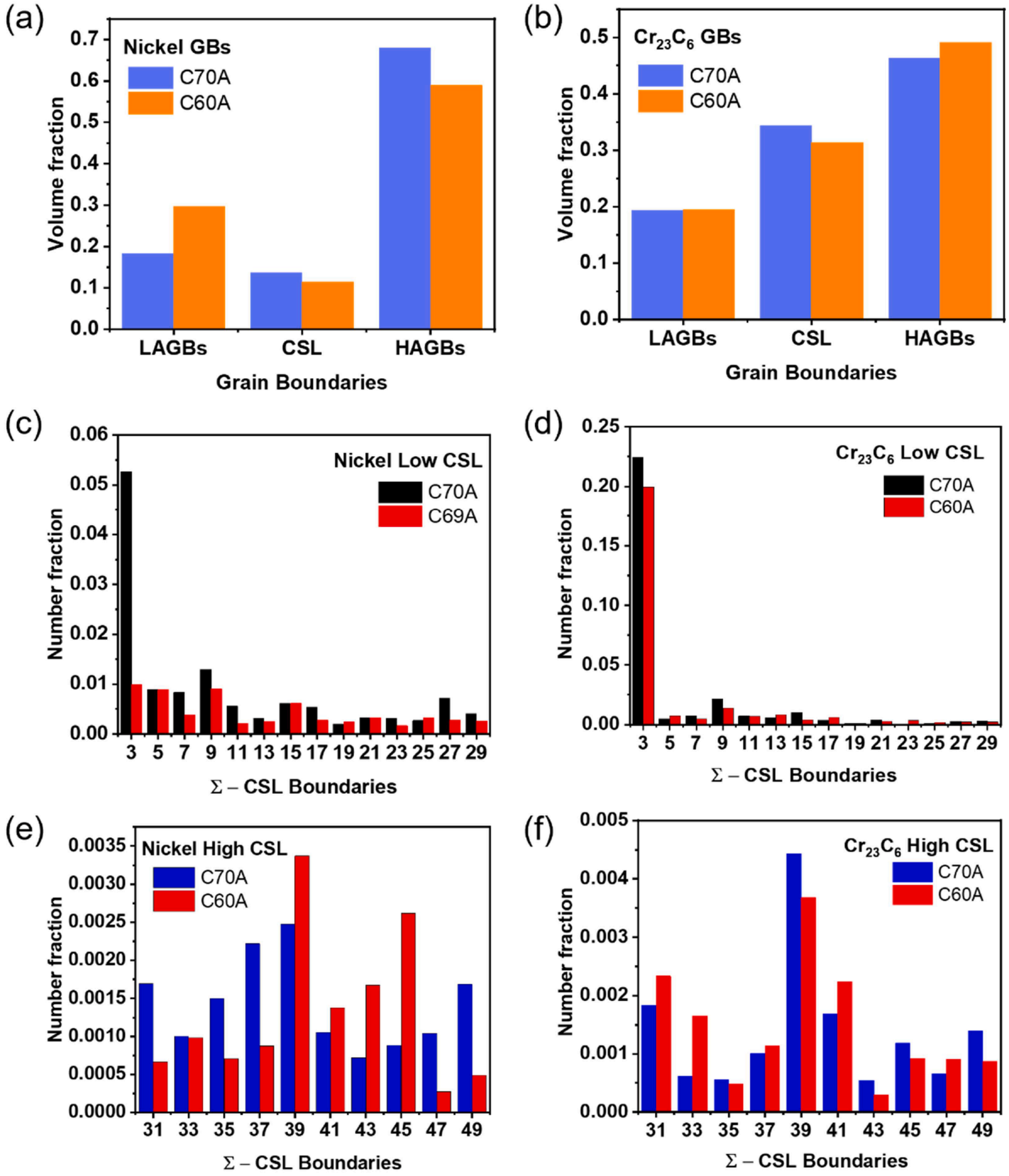

Fig. 8. Grain boundary character distribution (GBCD) analyses (a) volume fraction of Nickel grain boundaries, **(b)** volume fraction of $Cr_{23}C_6$ grain boundaries, **(c)** number fraction of low Nickel Σ-CSL boundaries ($3 < \sum < 29$), **(d)** number fraction of low $Cr_{23}C_6$ Σ-CSL boundaries ($3 < \sum < 29$), **(e)** number fraction of high Nickel Σ-CSL boundaries ($\sum > 29$), and **(f)** number fraction of high $Cr_{23}C_6$ Σ-CSL boundaries ($\sum > 29$).

denoted by the symbol sigma (Σ) [44]. Due to its reciprocity, lower values of Σ indicate higher degrees of order between lattices. An analysis focusing on the concentration of low Σ-CSL boundaries, specifically those with values $3 < \Sigma < 29$, was conducted in both the Nickel phase (Fig. 8**(c)**) and the $Cr_{23}C_6$ phase (Fig. 8**(d)**), as well as high Σ-CSL boundaries, denoted as $\Sigma > 29$, for the Nickel phase (Fig. 8**(e)**) and the $Cr_{23}C_6$ phase (Fig. 8**(f)**). High Σ-CSL boundaries are typically considered random and often render materials susceptible to intergranular corrosion [45,46]. However, the concentrations of these boundaries were found to be minimal in both coatings, suggesting a negligible correlation with high-angle boundary energy. On the other hand, the results indicate that Σ3 boundaries prevail in both phases of the coatings. The Σ3 boundary is categorized as a special boundary representative of twin boundaries [47]. In line with the Σ3 regenerative model proposed by Randle [48], other special boundaries are estimated by $\Sigma 3^n$, including $\Sigma < 29$ boundaries such as Σ5, Σ7, Σ11, Σ13, Σ15, Σ17, Σ19, Σ21, and Σ25 [49]. These represent common types of low CSL boundaries. All Σ3 and $\Sigma 3^n$ boundaries are reported to exhibit restricted responses to intergranular phenomena, making them desirable in processes such as stress corrosion cracking, creep, fatigue, wear, and corrosion resistance [50].

3.1.4. Geometrically necessary dislocation (GND) density

In materials with FCC structures, LAGB formation correlates directly with dislocation density [51]. Under high-strain conditions typical of load-bearing or wear-inducing applications, geometrically necessary dislocations (GNDs), estimated from the material's kernel average misorientation (KAM) values, migrate to energetically favorable positions, forming LAGBs to accommodate strain [52]. An analysis of GNDs within the γ-Ni and $Cr_{23}C_6$ phases is conducted to elucidate the influence of PTA current on GND density within the coatings.

Fig. 9 presents KAM maps representing the distribution of accumulated dislocation densities in the analyzed coatings. Black regions correspond to areas that were not indexed concerning the examined phase. In Fig. 9**(a)**, the all-phase inclusive KAM map of the C70A coating displays a statistical mode of KAM around 0.35°. Conversely, the KAM

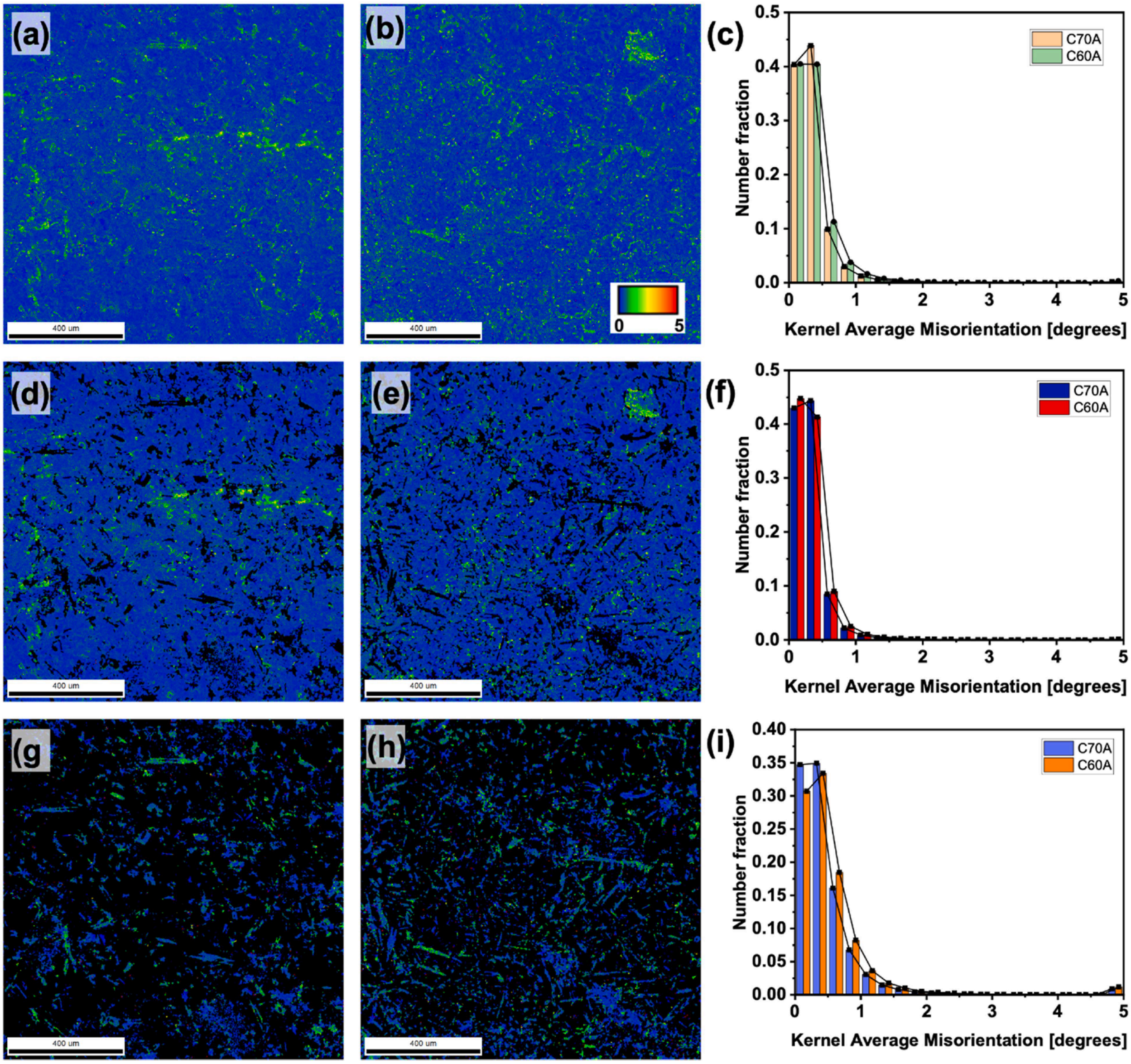

Fig. 9. Kernel average misorientation (KAM) maps (a) all-phase inclusive KAM map for C70A, **(b)** all-phase inclusive KAM map for C60A, **(c)** number fraction of KAM values for all phases in C70A and C60A, **(d)** KAM map of Nickel phase for C70A, **(e)** KAM map of Nickel phase for C60A **(f)** number fraction of KAM values for Nickel phase in C70A and C60A, **(g)** KAM maps of Cr23C6 phase for C70A, **(h)** KAM maps of Cr23C6 phase for C60A, and **(i)** number fraction of KAM values for C70A and C60A.

distribution for all phases in the C60A coating, depicted in Fig. 9**(b)**, exhibits a mode of approximately 0.38°. A comparison of KAM distributions for all phases between the C70A and C60A coatings is presented in Fig. 9**(c)**. For the γ-Ni phase, Fig. 9**(d)** shows a mode of KAM around 0.32° for the C70A coating, while Fig. 9**(e)** illustrates a mode of approximately 0.33° for the same phase in the C60A coating. The KAM distributions for the γ-Ni phase in both coatings are contrasted in Fig. 9 **(f)**. Regarding the $Cr_{23}C_6$ phase, the mode of KAM is about 0.47° for the C70A coating (Fig. 9**(g)**), whereas it reaches approximately 0.52° for the same phase in the C60A coating (Fig. 9**(h)**). A comparison of KAM dislocation distributions for the $Cr_{23}C_6$ phase in both coatings is shown in Fig. 9**(i)**. The computed geometrically necessary dislocation (GND) value for the coating prepared with a 70 A PTA current was found to be 1.08×10^{13} m^{-2}. Upon reducing the PTA current to 60 A, the GND value decreased to 1.04×10^{13} m^{-2}.

3.1.5. *Texture evolution*

Fig. 10 illustrates the orientation distribution functions (ODF) within the coatings, depicting sections representing various ODF orientations ($\varphi_2 = 0^\circ, 45^\circ$ and 65°) for the Nickel phase. **Supplementary Figure S2** provides detailed elaboration on the Nickel ODF for all texture components. At the ODF ($\varphi_2 = 0^\circ$) section, the C70A coating predominantly exhibits a brass texture (Bs) {110}<112>;(55,90,45) with a volume fraction of 10.75 % (**Figure 10(a)**). Additionally, a moderate presence of

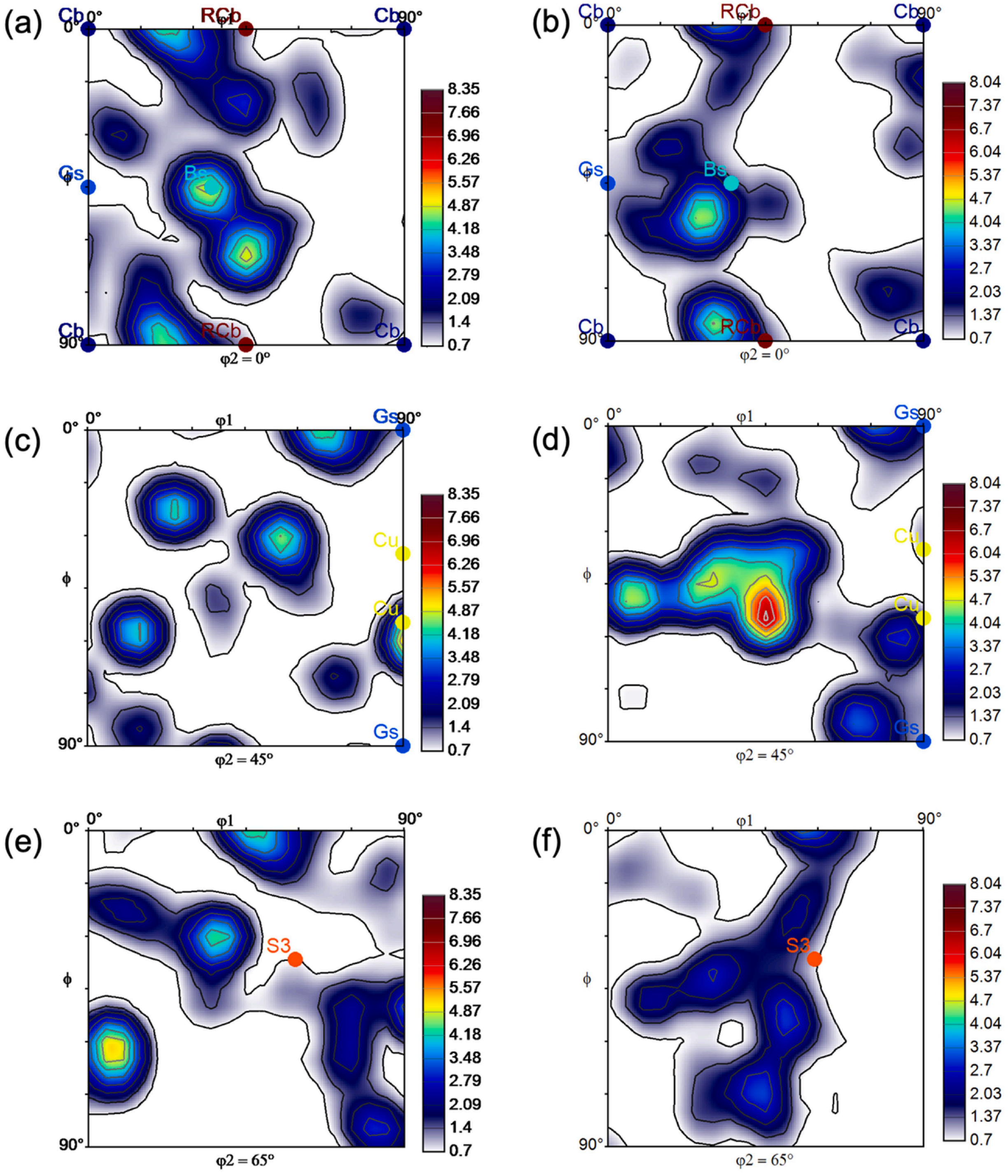

Fig. 10. Orientation distribution function (ODF) sections ($\varphi_2 = 0^\circ, 45^\circ$ and 65°) (a, c, e) C70A coating, and **(b, d, f)** C60A coating.

rotating cube texture (RCb) {001}<110>;(45,0,0) and cube texture (Cb) {001}<100>;(45,0,45) is observed, with volume fractions of 3.67 % and 5.61 % respectively. Furthermore, the goss texture (Gs) {011}<100>;(90,90,45) is detected, occupying a volume fraction of 3.91 %. Upon reducing the PTA current to 60 A, the C60A coating at the same ODF ($\varphi_2 = 0^\circ$) orientation (Fig. 10**(b)**) shows similar textures but with increased volume fractions. The Bs texture increases to 11.29 %, RCb texture to 7.87 %, Cb texture to 6.71 %, and Gs texture to 7.67 %. At ODF ($\varphi_2 = 45^\circ$), the C70A coating predominantly displays a copper texture (Cu) {112}<111>;(90,35,45) with a volume fraction of 1.87 % (Fig. 10**(c)**). This texture evolves in the C60A coating with a volume fraction of 3.25 % (Fig. 10**(d)**). Evolution of the γ fiber is evident at ODF ($\varphi_2 = 45^\circ$), in the {111} crystallographic plane. Additionally, the s texture (S3) {023}<634>;(59,37,63) is identified at ODF ($\varphi_2 = 65^\circ$) orientation, with volume fractions of 10.45 % in the C70A coating (Fig. 10**(e)**) and 13.05 % in the C60A coating (Fig. 10**(f)**).

Fig. 11 provides a comparative summary of the texture components for both coatings. The results reveal a consistent trend of FCC Nickel texture growth in the coatings when a lower PTA current of 60 A is used for deposition. This observation aligns with findings by Eghlimi et al. [53], indicating that lower heat input and faster cooling rates lead to stronger texture development in thermally deposited coatings, directly influencing fiber growth within the coatings. The S3 texture component facilitates the evolution of the Ni α fiber (**Figure S2**), while RCb and Cu texture components accelerate the development of the τ fiber in Nickel. In FCC metals, planes with {100} orientation exhibit relatively greater growth due to their lower planar densities and higher number of free sites. The enhanced texture growth observed, particularly when utilizing a lower PTA current, can be attributed to the solidification mode of the coating, primarily involving atom movement from the liquid molten clad to the solidified metal through (hkl) Miller indices. Faster cooling rates in the coating prepared with 60 A current facilitate greater proportions of free sites in crystal planes, fostering the evolution of texture components compared to the C70A coating with a relatively slower cooling rate.

3.2. *Corrosion resistance*

Fig. 12**(a)** illustrates the open circuit potential (E_{ocp}) curves obtained for the C70A and C60A coatings. Initially, the E_{ocp} values were approximately -381 mV vs. Ag/AgCl for the C70A coating and approximately -425 mV vs. Ag/AgCl for the C60A coating. Subsequently, there was a notable decrease in E_{ocp} values until stabilization occurred around 2600 s, reaching approximately -465 mV vs. Ag/AgCl for C70A and approximately -490 mV vs. Ag/AgCl for C60A. Such abrupt changes in E_{ocp} typically indicate uncontrolled alterations in the rates of either anodic or cathodic processes. In aqueous environments, surfaces of materials tend to form oxide films, leading to fluctuations in electrochemical activity and subsequently affecting E_{ocp} values. Fig. 12**(b)** illustrates Tafel plots depicting the corrosion potential (E_{corr}) of the coatings. Notably, the E_{corr} for the coating fabricated using a current of 70 A registered at -475 mV vs. Ag/AgCl, whereas for the 60 A condition, the E_{corr} was -495 mV vs. Ag/AgCl. Subsequent analysis yielded a corrosion current density of 34.3 μA/cm^2 for the 70 A coating, whereas a reduction to 25.10 μA/cm^2 was observed for the 60 A coating, marking a decrease of 26.8 %. Moreover, the polarization resistance (R_{pol}) was computed, yielding $R_{pol} = 699$ Ωcm^2 for the 70 A coating, and a higher resistance of $R_{pol} = 800$ Ωcm^2 for the 60 A coating. These results collectively suggest that the coating prepared with 60 A current demonstrates superior corrosion resistance, as inferred from the open circuit potential investigations.

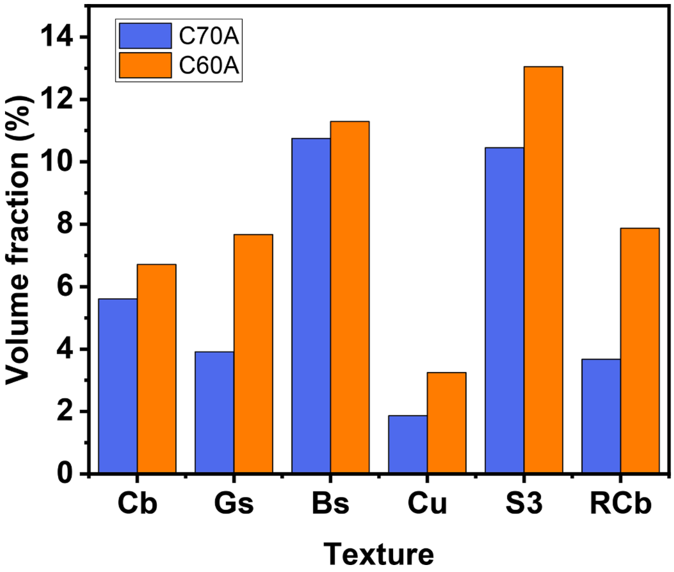

Fig. 11. Volume fraction of Nickel texture components in the coatings: Cb – Cube texture; **Gs** – Goss texture; **Bs** – Brass texture; **Cu** – Copper texture; **S3** – S texture; **RCb** – Rotating cube texture.

Electrochemical impedance spectroscopy (EIS) was used to investigate the complementary corrosion resistance of the coatings. Prior to measurement, the system was allowed to stabilize for 300 s to ensure a consistent electrochemical potential. The resulting data are presented in the Nyquist plot (Fig. 12**(c)**). Characteristic of Ni-matrix coatings, the Nyquist plots displayed prominent high-frequency semi-circular loops, indicative of charge transfer resistance within the coatings. The radii of these loops differed significantly between the coatings. Specifically, the coating fabricated with a 70 A current exhibited a maximum radius of 1375 Ωcm^2 along the imaginary axis, while the coating prepared with a 60 A current showed a notably larger maximum radius of 1875 Ωcm^2. Furthermore, the Bode spectra (Fig. 12**(d)**) depicted the frequency response of the coatings up to 100 kHz, revealing higher impedance for the coating produced with a 60 A current compared to its 70 A counterpart. These findings from EIS analysis underscore the enhanced corrosion resistance of the coating fabricated with a 60 A current, corroborating its superiority over the 70 A counterpart.

3.3. *Hardness and tribological behavior*

Vickers microhardness measurements were conducted across the cross-section of plasma transferred arc welding (PTAW) deposited coatings from the topcoat into the substrate material. This investigation adhered to a systematic measurement regime, as depicted in **supplementary Figure S3**, encompassing three distinct regions: the coating middle zone (MZ), the interface including the transition zone (TZ) and the coarse-grained heat-affected zone (CGHAZ), and finally the substrate, situated proximal to the base material's bottom. Measurements were carried out at ambient temperature after metallographic polishing to attain a mirror surface. The resulting microhardness maps are presented in Fig. 13**.** Within the MZ of the C70A coating (Fig. 13**(a)**), the average microhardness measured 475.2 $HV_{0.5}$, with a standard deviation of 55.7. Conversely, at the interface (Fig. 13**(b)**), the TZ displayed a reduced average microhardness of 450.5 $HV_{0.5}$, with a standard deviation of 60.3. The CGHAZ exhibited a mean microhardness of 209.9 $HV_{0.5}$, with a standard deviation of 11.8. Microhardness at the substrate's bottom (Fig. 13**(c)**) measured 195.7 $HV_{0.5}$, with a standard deviation of 9.5. This suggests a microhardness increase of approximately 6.6 % in the heat-affected zone post-coating solidification, attributable to the presence of lath martensite in this region following solidification.

Comparatively, the coating prepared with a lower PTA current of 60 A demonstrated superior microhardness over its 70 A counterpart. The MZ of the former (Fig. 13**(d)**) exhibited an average microhardness of 636.1 $HV_{0.5}$, with a standard deviation of 66.9. Despite non-uniform microhardness distribution within the MZ due to the heterogeneous Cr-rich dendritic structure, the maximum microhardness recorded was

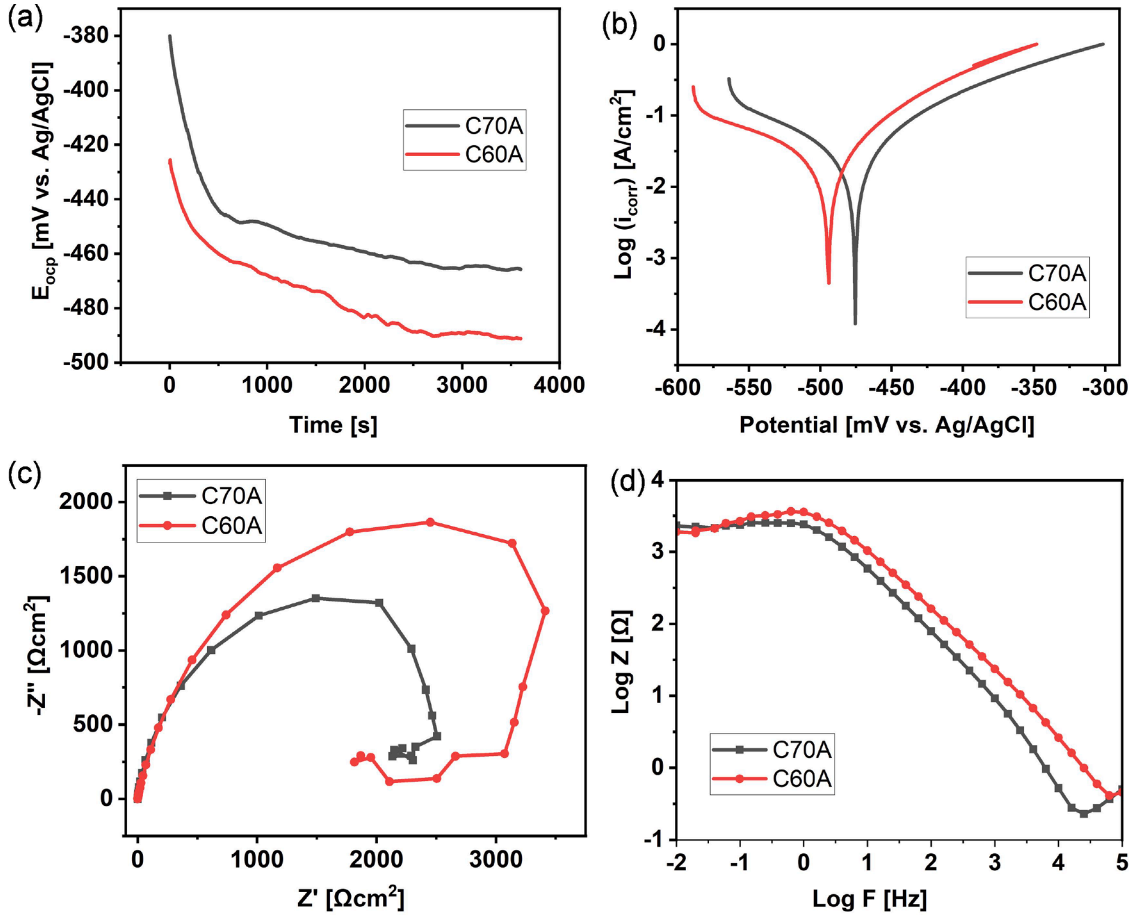

Fig. 12. **Corrosion resistance properties (a)** Open circuit potential, **(b)** Tafel plots, **(c)** Nyquist EIS curves, and **(d)** EIS bode spectra.

estimated at 754.0 HV$_{0.5}$, ranking among the highest reported for as-sprayed PTAW deposited NiCrBSi coatings. Other studies have reported microhardness values in the range of 600 to 750 HV for such coatings prepared by PTAW technology [33,54],. At the interface (Fig. 13**(e)**), the TZ registered an average microhardness of 659.1 HV$_{0.5}$, with a standard deviation of 26.9. The CGHAZ displayed an average microhardness of 234.1 HV$_{0.5}$, with a standard deviation of 43.3. Analogous to the 70 A current coating, the region adjacent to the base material's bottom for the 60 A current coating (Fig. 13**(f)**) exhibited the lowest microhardness, measuring 176.7 HV$_{0.5}$, with a standard deviation of 10.1.

Fig. 14**(a)** depicts the temporal evolution of the coefficient of friction (COF) as measured during wear resistance tests, as a function of sliding wear distance. Initially, both coatings display substantial fluctuations in COF, which gradually stabilize after approximately 70 m of sliding distance. These fluctuations are attributed to the presence of inhomogeneities within the coatings encountered by the testing apparatus. Two primary factors contribute to these inhomogeneities. Firstly, the turbulent nature of the plasma jet during the coating process can result in the presence of unmelted powder particles, thereby diminishing the likelihood of complete particle fusion. Secondly, fluctuations may arise from surface wear mechanisms. For instance, if wear occurs via delamination or fatigue wear, debris from this process can augment surface roughness, leading to COF fluctuations. The coating prepared with a 70 A current exhibits a COF of 0.60 ± 0.02, whereas its counterpart prepared with a 60 A current displays a COF of 0.5 ± 0.01.

Fig. 14**(b)** is a comparison of volume losses incurred by both coatings after wear tests, along with an analysis of wear track dimensions, providing insights into wear extent. Notably, the coating fabricated with a 60 A current demonstrates lower volume loss (2.3 ± 0.1 m^3) and a narrower wear track width (564 μm) compared to the coating prepared with a 70 A current, which exhibits a larger volume loss (3.7 ± 0.1 m^3) and a wider wear track width (1151 μm). Utilizing Archard's law, the wear rate is derived from volume loss and COF values (Eqs. 4 **and** 5). Accordingly, the wear rate of the coating fabricated with a 70 A current is calculated to be greater at $3.74 \pm 0.11 \times 10^{-2}$ m^3/m, surpassing the wear rate of the 60 A coating, which registers a wear rate of $2.32 \pm 0.12 \times 10^{-2}$ m^3/m. These findings establish the lower PTA current of 60 A to produce NiCrBSi coatings with superior wear resistance, over the coating produced with 70 A PTA current.

The investigation into the wear mechanism was undertaken using a combination of digital microscopy, SEM, and EDS techniques. Fig. 15**(a)** presents the digital micrograph portraying the surface of the C70A coating before undergoing wear testing. After wear tests, Fig. 15**(b)** shows that the C70A coating exhibited a noticeably expanded wear track measuring approximately 1151 μm. Upon closer examination of the wear track under the SEM, two primary regions of wear emerged: delamination wear (D$_L$) and abrasive wear grooves (A$_G$), as illustrated in Fig. 15**(c)**. Examination of the wear track revealed an accumulation of wear debris (Fig. 15**(d)**) generated between the coating material and counter body during the wear test, promoting delamination wear. Chemical composition analysis via EDS revealed that the wear debris shared the same chemical composition as the coating, indicating negligible wear of the counter body. This observation can be attributed to the counter body's hardness, specifically the ZrO_2 G28 ball, which possesses a marked minimum hardness of 940 HV, significantly higher than the coatings' maximum hardness of 754 HV. Delamination wear is characterized by profound ploughing of the contact surface leading to material removal. **Figure 15(e)** demonstrates that in the delamination and abrasive wear regions, Fe and Ni do not overlap, further corroborating

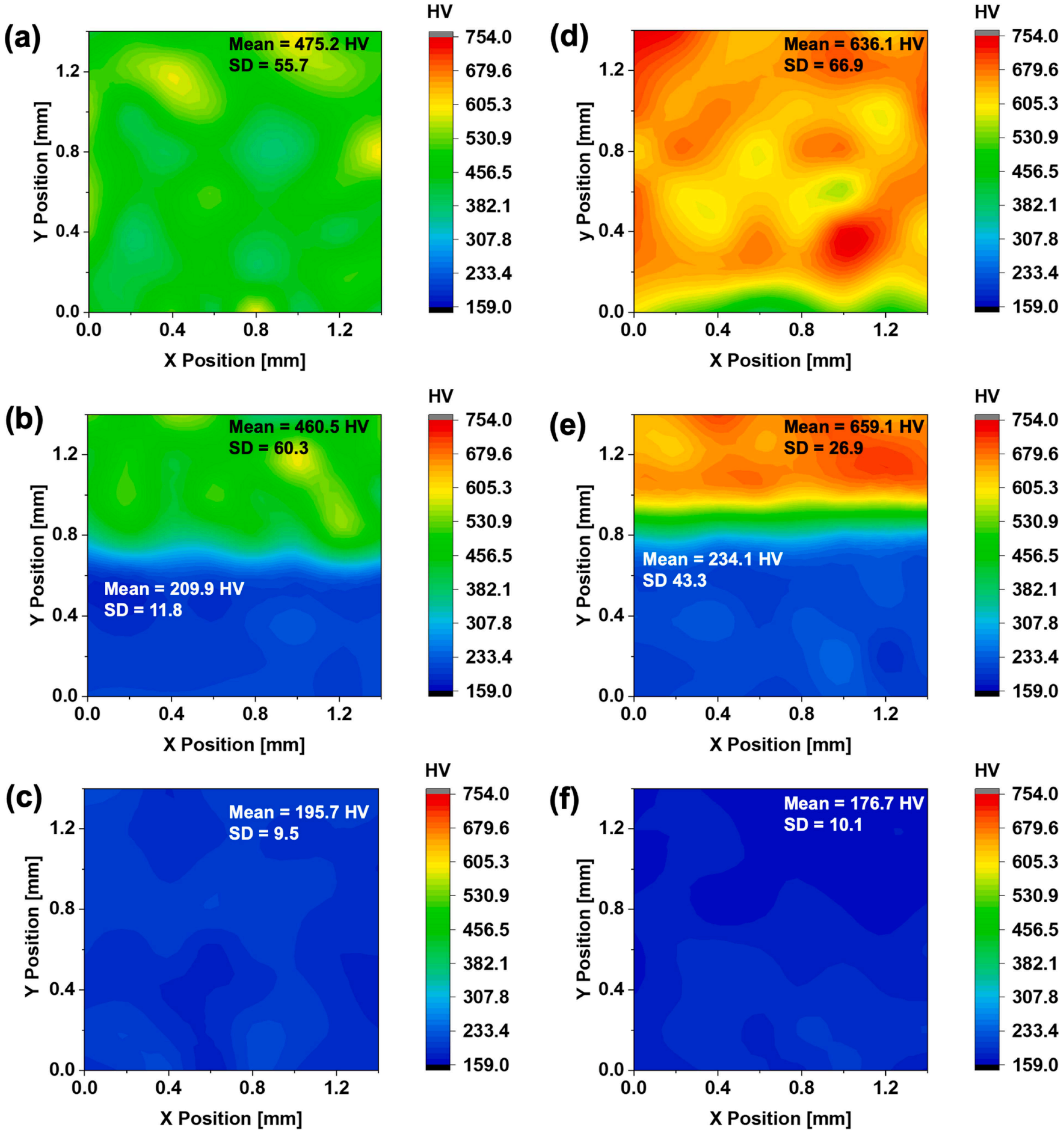

Fig. 13. Microhardness (HV) of the cross-section of the coatings **(a)** HV of C70A coating MZ, **(b)** HV of C70A interface, **(c)** HV of C70A substrate, **(d)** HV of C60A coating MZ, **(e)** HV of C60A interface, and **(f)** HV of C60A substrate.

the co-occurrence of both wear mechanisms in the C70A coating [55].

Fig. 16**(a)** presents the digital micrograph of the surface of the C60A coating before wear testing. Following wear tests, the wear track in this coating exhibited an evidently smaller width of approximately 564 µm (Fig. 16**(b)**). Similar to the C70A coating, Fig. 16**(c)** illustrates that the C60A coating displays regions of delamination wear and abrasive wear grooves. EDS analysis similarly indicates the concurrence of both delamination and abrasive wear mechanisms in the wear track.

The abrasive grooves in the C60A coating showed a larger volume compared to those observed in the coating fabricated under a higher PTA current of 70 A. This dissimilarity suggests that during wear testing of the C60A coating, initial material removal from the surface triggered delamination wear zones. However, as wear debris continued to accumulate, proximity to chromium carbide phases prevalent in the microstructure of this coating increased. This proximity facilitated reduced friction between the counter piece and the coating, thereby accentuating the formation of abrasive grooves as the dominant wear feature within the central part of the C60A coating's wear track. However, unique to the C60A coating's wear track, there were observed regions of crack initiation with branching pattern (Fig. 16**(d)**), signifying the presence of fatigue wear mechanism in this coating.

4. Discussion

The utilization of low plasma transferred arc currents, typically below 100 A, in the preparation of coatings tailored for applications demanding high wear and corrosion resistance often entails notable challenges. These challenges commonly manifest as incomplete powder

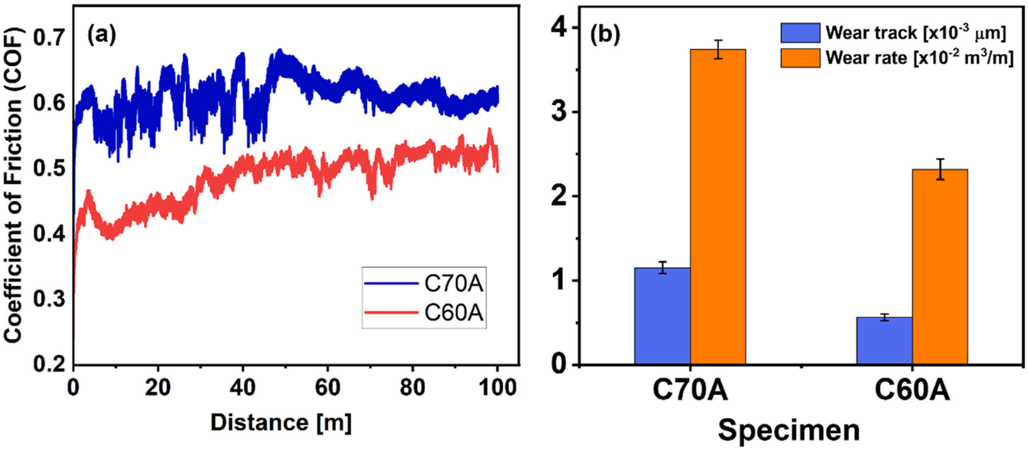

Fig. 14. Tribological properties (a) Coefficient of friction, and **(b)** comparison of the width of the sliding wear track and wear volume losses of the coatings.

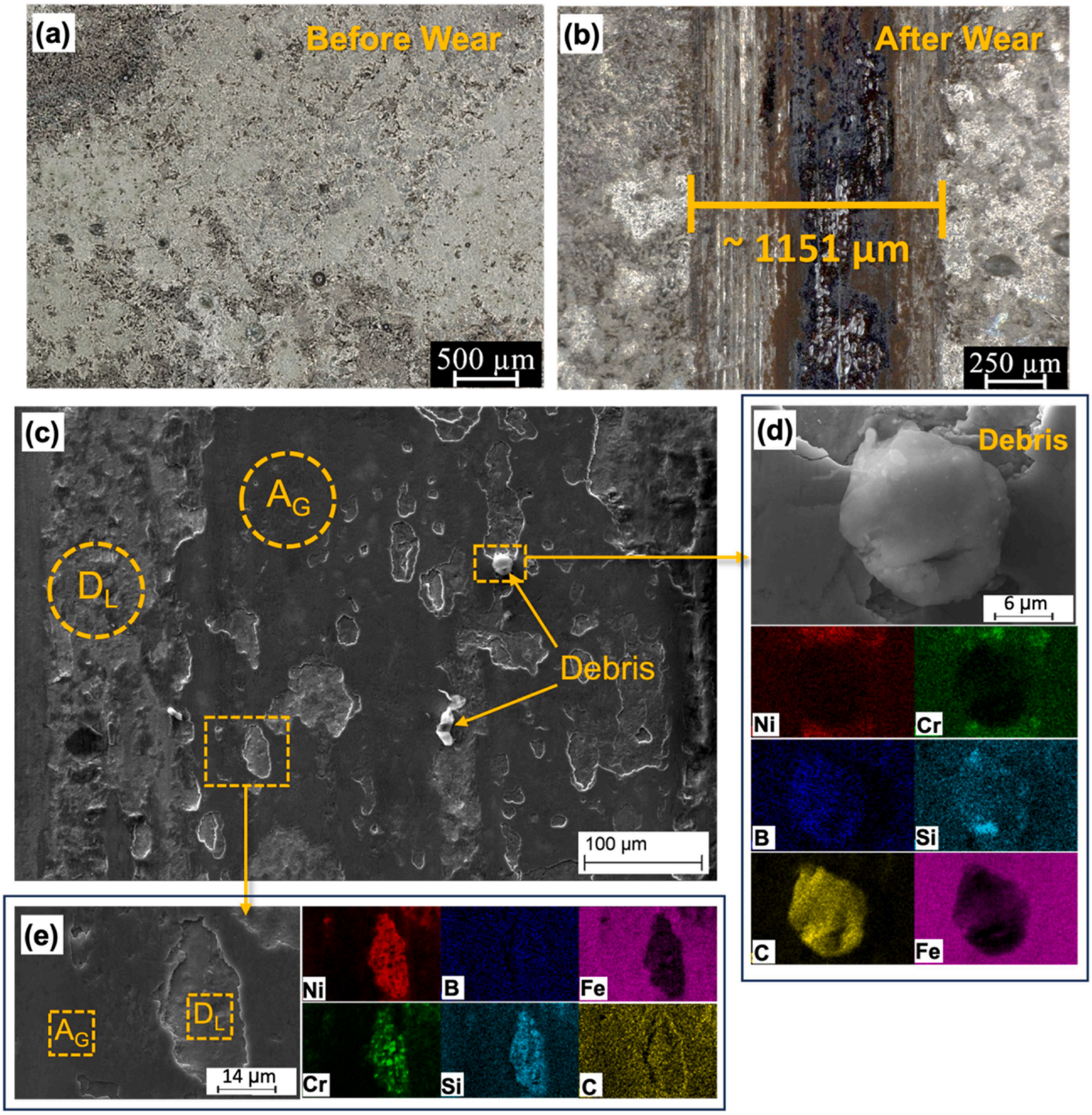

Fig. 15. Micrographs of the surface of the C70A coating before and after wear resistance tests (a) Digital image of the surface of C70A coating before wear test, **(b)** digital image of the surface of C70A coating after wear test, **(c)** SEM image of the wear track of C70A showing regions of wear and debris, **(d)** SEM image of wear debris with corresponding EDS chemical composition maps, and **(e)** SEM image of the two main regions of wear with corresponding EDS chemical composition maps. **A_G – Abrasive groove; D_L – Delamination wear.**

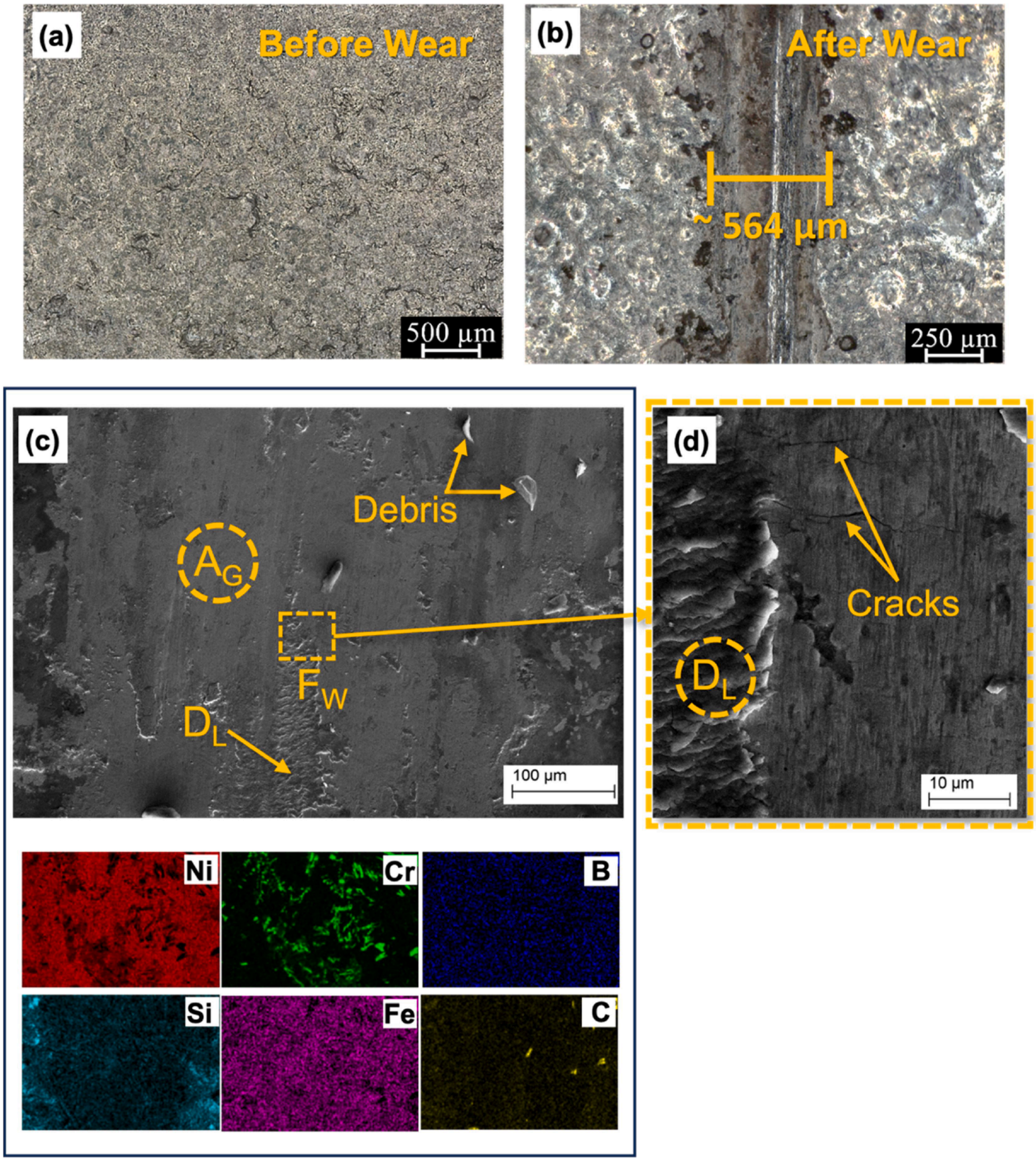

Fig. 16. Micrographs of the surface of the C60A coating before and after wear resistance tests (a) Digital image of the surface of C60A coating before wear test, **(b)** digital image of the surface of C60A coating after wear test, **(c)** SEM image of the wear track of C60A showing regions of wear and debris, (d) SEM image of wear debris with corresponding EDS chemical composition maps, and (e) SEM image of the two main regions of wear with corresponding EDS chemical composition maps. **A_G – Abrasive groove; D_L – Delamination wear; F_W – Fatigue wear.**

fusion, elevated porosity, or the formation of numerous crack sites within the resulting coatings, ultimately compromising their corrosion and tribological properties. However, through a novel approach combining a low plasma torch standoff distance of 5 mm with low arc currents (70 A and 60 A), this study demonstrates the successful fabrication of NiCrBSi coatings onto a 15HM steel substrate with enhanced corrosion and tribological properties. The coatings are characterized by the prevalence of face-centered cubic (FCC) strengthening phases γ-Ni and chromium carbide ($Cr_{23}C_6$), alongside minor concentrations of orthorhombic structured Cr_3C_2 phases. The phases possess low symmetry, whose behavior and characteristics in the coatings influence the resulting properties. The dominant γ-Ni phase possesses evolved Ni FCC texture components including brass texture (Bs) {110}<112>;(55,90,45), rotating cube texture (RCb) {001}<110>;(45,0,0), cube texture (Cb) {001}<100>;(45,0,45), goss texture (Gs) {011}<100>;(90,90,45), copper texture (Cu) {112}<111>;(90,35,45), and the s texture (S3) {023}<634>;(59,37,63) occurring at orientation distribution functions (ODF) ($\varphi_2 = 0^\circ,\ 45^\circ$ and 65°).

The initiation of corrosion within Ni-based coatings frequently occurs through a spontaneous chemical reaction, wherein the surface morphology plays a pivotal role [56]. Nevertheless, examination of Figs. 15**(a)** and 16**(a)** reveals that the surfaces of the fabricated coatings exhibit an absence of surface defects. Although surface defects accelerate the corrosion process, nonetheless, the ingress of electrolytic corrosive medium permeates the coating from the surface towards the coating-substrate interface. However, the velocity of penetration is notably influenced by various factors, including grain boundaries, texture, and geometrically necessary dislocations (GNDs) along the cross-sectional plane of the coating. Grain boundaries play a pivotal role in regulating intergranular corrosion. Special low Σ-CSL boundaries like the Σ3 boundary, and low-angle grain boundaries (LAGBs), characterized by low energies, decelerate corrosion rates, while texture components dictate transgranular (bulk) corrosion behavior [57–59].

Within the framework of the FCC system, {111} planes exhibit dense packing, inherently manifesting heightened resistance to corrosion, with {100} and {110} planes following suit. XRD analysis reveals the highest intensity peak corresponding to the {111} plane of the γ-Ni phase, particularly accentuated in the C60A coating. Notably, the evolution of the γ fiber, from the {111} crystallographic plane, bordered by orientation distribution functions ODFs {111}>110>;(0,55,45) and {111}>112>;(90,55,45) at $\varphi_2 = 45^\circ$, as shown in supplementary **Fig. S2**, positions it to possess superior transgranular properties compared to the other Ni fibers. In a notable study, He et al. [60] explored the microstructural evolution of interstitial free steels, identifying the γ fiber as the dominant recrystallized texture component. They observed elevated corrosion resistance and they attributed it to the increase in the volume fraction of the γ fiber upon annealing. Similarly, Fu et al. [61] corroborate the substantial contributions of the γ fiber and the dense packing of the {111} plane in the FCC system towards augmenting intergranular properties and overall performance of FCC structured materials. Thus, the observation of higher volume fractions of evolved texture components in the C60A coating, along with elevated intensity XRD peaks corresponding to the γ-Ni phase, establishes a basis for understanding the superior corrosion and wear resistance properties of the C60A coating compared to the C70A coating. Similarly, texture analyses reveal that the brass texture (Bs) components corresponding to the (110) plane are oriented towards the surface of the coatings, with a higher concentration observed in the coating fabricated under a current of 60 A. Likewise, the rotating cube texture (RCb) component in the coating prepared with 60 A current exhibits double the concentration compared to the coating prepared with 70 A. According to Mukherjee et al. [62], the RCb texture component arises from grain rotation aligned with the direction of coating application. Coupled with the relatively shallow weld pool associated with low PTAW currents (i.e., currents below 100 A), this results in low Lorentz and high Marangoni forces, fostering grain growth along the ⟨101⟩ and ⟨111⟩ directions [63]. Consequently, the heightened concentrations of FCC texture components in the 60 A coating inherently endow it with greater resistance to impeding the penetration of the electrolyte.

The GND density within the coating fabricated under 70 A current was found to be greater at 1.08×10^{13} m^{-2} compared to the value of 1.04×10^{13} m^{-2} in the coating prepared with 60 A current. According to existing literature [45,64–66], higher GND density exacerbates corrosion by promoting localized corrosion, particularly pitting corrosion. Consequently, electrolyte accumulation transpires within these pits, fostering the intergranular diffusion of metal ions towards the material-oxide film interface, thereby accelerating the corrosion rate. Electrochemical impedance spectroscopy (EIS) and Tafel investigations affirm the coating prepared with 60 A current as possessing superior corrosion resistance compared to the 70 A counterpart.

The tribological characteristics of NiCrBSi coatings exhibit substantial dependence on the properties of strengthening phases, encompassing texture type, orientation, and grain refinement within the coating structure [46,67],. The evolution of texture orientation plays a pivotal role in dictating the mechanical attributes of Ni-based coatings. According to Li et al. [68], ⟨100⟩ texture components, such as the cube and goss texture components, are associated with the lowest stress-strain energy density, consequently augmenting the mechanical robustness of FCC coatings, including hardness and wear resistance.

Furthermore, the evolution of grain size directly impacts the mechanical properties of the coatings [69], aligning with the Hall-Petch theory [50]. EBSD analysis showcased enhanced grain refinement in coatings produced with reduced production current, transitioning from 70 A to 60 A. Notably, the microhardness of the C60A-coated sample (636.1 ± 66.9 HV$_{0.5}$) was significantly higher than its C70A counterpart (475.2 ± 55.7 HV$_{0.5}$), showing a remarkable improvement of approximately 40 % ($p < 0.001$). This enhancement can be attributed to the heightened concentration of texture components and grain refinement observed within the coating produced at 60 A. Archard's law [70] postulates an inverse relationship between hardness and wear rate, which finds validation in this study. The wear rate of the coating prepared with 60 A current was found to be significantly lower (approximately 38 %) than that of the 70 A counterpart ($p < 0.01$), underscoring the direct correlation between elevated hardness and enhanced wear resistance, as documented in existing literature [13,14].

4.1. *Influence of process current on solidification thermodynamics and kinetics*

The primary effect of reducing the PTAW current from 70 A to 60 A is a reduction in the total heat input. The C70A coating, with its higher heat input, experienced a slower cooling rate, evidenced by its larger dendrite arm spacing (37.4 μm). Conversely, the lower heat input for the C60A coating led to a faster cooling rate and a finer DAS (23.01 μm), indicating more rapid solidification. This difference in cooling rate is the critical factor that dictates the thermodynamics and kinetics of phase formation. The principles explored in this section are on the basis of Tsallis' generalization of the ordinary Boltzmann-Gibbs theories [71–75], and supported by classical nucleation thermodynamics [76–79].

The thermodynamic driving force for solidification, which is the change in Gibbs free energy per unit volume, ΔG_v, is a function of the undercooling, ΔT (where $\Delta T = T_m - T$; T_m is the equilibrium melting temperature). This relationship can be approximated by Eq. 6.

$$\Delta G_v = \frac{\Delta H_f \Delta T}{T_m} \tag{6}$$

where ΔH_f is the latent heat of fusion. Eq. (6) shows that the faster cooling rate of the C60A process creates a larger undercooling (ΔT), which in turn generates a stronger thermodynamic driving force (a more negative ΔG_v) for the liquid-to-solid transformation.

However, for a new, stable solid grain to form, a kinetic energy barrier for nucleation, ΔG^*, must be overcome. For homogeneous nucleation, this barrier is inversely related to the square of the driving force (Eq. 7):

$$\Delta G^* = \frac{16\pi\gamma_{s\leftrightarrow l}^3}{3(\Delta G_v)^2} \tag{7}$$

where $\gamma_{s\leftrightarrow l}$ is the solid-liquid interfacial energy. The most significant information derived from Eq. (7) is that the stronger driving force in the C60A sample (from its larger ΔT) leads to a significant reduction in the energy barrier for nucleation.

This reduction in the kinetic barrier has an exponential effect on the nucleation rate, $\dot{N}$, which is the number of new grains forming per unit volume per unit time. The rate is described by the Arrhenius-type equation (Eq. 8):

$$\dot{N} = K_1 \exp\left(-\frac{\Delta G^*}{k_B T}\right) \tag{8}$$

where K_1 is a pre-exponential factor related to atomic mobility and k_B is the Boltzmann constant. As shown in Eq. (8), the nucleation rate is exponentially sensitive to the energy barrier ΔG^*. Therefore, the substantially lower barrier in the C60A process resulted in an exponentially higher nucleation rate. This massive increase in the rate of new grain formation is the fundamental reason for the grain refinement observed in the C60A coating, where the average grain size was reduced to 14.3 μm compared to 16.6 μm in the C70A sample.

In contrast, the slower cooling of the C70A sample resulted in less undercooling, a higher nucleation barrier (ΔG^*), and a much lower nucleation rate ($\dot{N}$). This gave atoms more time to diffuse to existing grains, favoring grain growth over the formation of new grains, leading to the coarser final microstructure.

4.2. Limitations of the study and future work

Although the scope of this study has been explicitly outlined in the introduction section, the authors acknowledge certain limitations in the present study which open avenues for future research. Firstly, this study focused on a specific standoff distance (5 mm) and two current levels (60 A and 70 A). While this allowed for a detailed investigation, the findings may not be directly generalizable to other PTAW parameters. Future work could explore a wider processing window, including different standoff distances and a broader range of currents, to establish a more comprehensive processing map.

Additionally, the study was limited to the NiCrBSi alloy on a low alloy steel substrate. The generalizability of the results to other coating-substrate systems needs to be investigated.

Furthermore, the corrosion and wear tests, while providing valuable data, have their limitations. Potentiodynamic polarization is an accelerated test, and the results may not perfectly correlate with long-term performance in real-world environments. Similarly, the ball-on-plate wear test represents a specific contact condition. Future studies could employ complementary techniques like long-term immersion tests, salt spray tests, and different wear test configurations (e.g., Taber abrasion, pin-on-disk) to obtain a more holistic understanding of the coating's performance.

Most importantly, the observation of fatigue cracking in the C60A coating during wear testing highlights a potential issue with its long-term durability under dynamic loads. Further investigation into the fatigue behavior of these coatings is warranted. Mitigation strategies such as post-deposition heat treatments or the use of a functionally graded interlayer could be explored to improve fatigue resistance.

5. Conclusions

This study successfully demonstrated a novel processing route for fabricating high-performance NiCrBSi coatings using low-current PTAW. By employing a low standoff distance of 5 mm, it was possible to produce dense, well-bonded coatings at 60 A and 70 A. The key findings are as follows:

- The coating produced at 60 A (C60A) exhibited a more refined microstructure with a smaller average grain size (14.3 μm) compared to the 70 A coating (C70A) (16.6 μm).
- The C60A coating showed superior mechanical properties, with a maximum microhardness of 754.0 HV0.5 and a 38 % lower wear rate than the C70A coating.
- The corrosion resistance of the C60A coating was significantly enhanced, as evidenced by a 26.8 % reduction in corrosion current density compared to the C70A coating.
- EBSD analysis revealed that the improved performance of the C60A coating is correlated with a higher volume fraction of beneficial FCC texture components, a greater proportion of low-angle grain boundaries, and a lower density of geometrically necessary dislocations.
- This study provides a promising and cost-effective method for engineering the microstructure of Ni-based coatings to achieve superior performance for demanding industrial applications.
- Performance assessment revealed superior properties in the coating fabricated with 60 A, including higher corrosion resistance, wear resistance, and hardness. Notably, the maximum hardness recorded for the 60 A coating was 754 $HV_{0.5}$, which stands among the highest reported values in literature for PTAW deposited NiCrBSi coatings.

CRediT authorship contribution statement

Augustine Nana Sekyi Appiah: Writing – review & editing, Writing – original draft, Project administration, Methodology, Investigation, Funding acquisition, Formal analysis, Data curation, Conceptualization. **Przemysław Snopiński:** Writing – review & editing, Formal analysis, Data curation. **Marek Pagáč:** Writing – review & editing, Supervision, Formal analysis. **Yao Mawuena Tsekpo:** Writing – review & editing, Investigation, Data curation. **Benjamin Agyei-Tuffour:** Writing – review & editing, Supervision. **Gilmar F. Batalha:** Writing – review & editing, Supervision, Resources. **Marcin Adamiak:** Writing – review & editing, Supervision, Resources, Conceptualization.

Declaration of competing interest

The authors declare that they have no known competing financial interests or personal relationships that could have appeared to influence the work reported in this paper.

Acknowledgement

This paper was completed in connection with the project „Innovative and additive technologies for sustainable energy industry", registration no. CZ.02.01.01/00/23_021/0010117 financed by the Structural Funds of European Union project.

Additionally, this work has been supported by funding from the European Union's Horizon programme under the MSCA Staff Exchanges Grant Agreement No. 101129996, SynAM project, and co-funded by the Minister of Science and Higher Education's programme "PMW" for the years 2024–2027, contract No. 5783/HE/2024/2.

Supplementary materials

Supplementary material associated with this article can be found, in the online version, at doi:10.1016/j.materresbull.2025.113653.

Data availability

Data will be made available on request.

References

[1] M.A. Shaikh, M. Hadjikakou, O. Geyik, B.A. Bryan, Assessing global agri-food system exceedance of national cropland limits for linking responsible consumption and production under SDG 12, Ecol. Econ. 215 (2024) 107993, https://doi.org/10.1016/j.ecolecon.2023.107993.

[2] M.A. Rosen, H.A. Kishawy, Sustainable manufacturing and design: Concepts, practices and needs, Sustainability 4 (2) (2012) 154–174.

[3] D. Garbiec, P. Siwak, Microstructural evolution and development of mechanical properties of spark plasma sintered WC–Co cemented carbides for machine parts and engineering tools, Arch. Civ. Mech. Eng. 19 (1) (2019) 215–223, https://doi.org/10.1016/j.acme.2018.10.004.

[4] A. Czupryński, Microstructure and abrasive wear resistance of metal matrix composite coatings deposited on steel grade AISI 4715 by powder plasma transferred arc welding part 1. Mechanical and structural properties of a cobalt-based alloy surface layer reinforced with particles of titanium carbide and synthetic metal–diamond composite, Materials 14 (9) (2021) 2382.

[5] X. Cheng, K. Chen, Y. Su, Green innovation in oil and gas exploration and production for meeting the sustainability goals, Resour. Policy 87 (2023) 104315, https://doi.org/10.1016/j.resourpol.2023.104315.

[6] I. Masudin, N. Tsamarah, D.P. Restuputri, T. Trireksani, H.G. Djajadikerta, The impact of safety climate on human-technology interaction and sustainable development: Evidence from Indonesian oil and gas industry, J. Clean. Prod. 434 (2024) 140211, https://doi.org/10.1016/j.jclepro.2023.140211.

[7] A. Amanov, S.P. Berkebile, Enhancement of sliding wear and scratch resistance of two thermally sprayed Cr-based coatings by ultrasonic nanocrystal surface modification, Wear 512–513 (2023) 204555, https://doi.org/10.1016/j.wear.2022.204555.

[8] T. Poloczek, A. Lont, J. Górka, The structure and properties of laser-cladded inconel 625/TiC composite coatings, Materials 16 (3) (2023) 1265.

[9] Y. Fu, et al., Fe-Co-based coating with high hardness and high saturation magnetization deposited by co-axial powder feeding plasma transferred arc

welding, Mater. Lett. 315 (2022) 131928, https://doi.org/10.1016/j.matlet.2022.131928.

[10] M. Adamiak, A.N.S. Appiah, R. Żelazny, G.F. Batalha, A. Czupryński, Experimental Comparison of Laser Cladding and Powder Plasma Transferred Arc Welding Methods for Depositing Wear-Resistant NiSiB+ 60 % WC Composite on a Structural-Steel Substrate, Materials 16 (11) (2023) 3912.

[11] A.N.S. Appiah, et al., Microstructure and performance of NiCrBSi coatings prepared by modulated arc currents using powder plasma transferred arc welding technology, Appl. Surf. Sci. 648 (2024) 159065, https://doi.org/10.1016/j.apsusc.2023.159065.

[12] A. Czupryński, Microstructure and Abrasive Wear Resistance of Metal Matrix Composite Coatings Deposited on Steel Grade AISI 4715 by Powder Plasma Transferred Arc Welding Part 2. Mechanical and Structural Properties of a Nickel-Based Alloy Surface Layer Reinforced with Particles of Tungsten Carbide and Synthetic Metal–Diamond Composite, Materials 14 (11) (2021) 2805, https://doi.org/10.3390/ma14112805.

[13] A.N.S. Appiah, O. Bialas, A. Czupryński, M. Adamiak, Powder Plasma Transferred Arc Welding of Ni-Si-B+ 60 wt % WC and Ni-Cr-Si-B+ 45 wt % WC for Surface Cladding of Structural Steel, Materials (Basel) 15 (14) (2022) 4956.

[14] A.G. Momin, B.C. Khatri, U. Shah, J. Valaki, Parameters for cladding using plasma transfer arc welding–A critical, Mater. Today Proc 77 (2023) 614–618.

[15] C. Guoqing, F. Xuesong, W. Yanhui, L. Shan, Z. Wenlong, Microstructure and wear properties of nickel-based surfacing deposited by plasma transferred arc welding, in: Proc. 8th Asian-Eur. Int. Conf. Plasma Surf. Eng. AEPSE 2011 228, 2013, pp. S276–S282, https://doi.org/10.1016/j.surfcoat.2012.05.125.

[16] S. Zhang, S. Wang, C.L. Wu, C.H. Zhang, M. Guan, J.Z. Tan, Cavitation erosion and erosion-corrosion resistance of austenitic stainless steel by plasma transferred arc welding, Eng. Fail. Anal. 76 (2017) 115–124, https://doi.org/10.1016/j.engfailanal.2017.02.007.

[17] A.E. Ikpe, O. Ikechukwu, and E. Ikpe, “Effects of arc voltage and welding current on the arc length of tungsten inert gas welding (TIG),” 2017.

[18] P. Gao, et al., Influence of Plasma Arc Current on the Friction and Wear Properties of CoCrFeNiMn High Entropy Alloy Coatings prepared on CGI through plasma transfer arc cladding, Coatings 12 (5) (2022) 633.

[19] L. Wang, et al., Fabrication of Fe–30Al alloy using plasma arc welding powered twin-wire directed energy deposition-arc process: Droplet transfer, microstructure, and mechanical property investigation, Intermetallics 161 (2023) 107961, https://doi.org/10.1016/j.intermet.2023.107961.

[20] F.W.C. Farias, et al., In situ interlayer hot forging arc plasma directed energy deposition of Inconel® 625: microstructure evolution during heat treatments, J. Alloys Compd. 952 (2023) 170059, https://doi.org/10.1016/j.jallcom.2023.170059.

[21] H.B. Mamo, et al., Prototyping Ti2Cu intermetallic grain growth heterogeneously in Ti6Al4V matrix through laser additive manufacturing, Mater. Des. 246 (2024) 113312, https://doi.org/10.1016/j.matdes.2024.113312.

[22] M. Bakalli, P. Keil, W. Strunz, T. Broeker, R. Herrmann, J. Vogelsang, Critical view of the results of the 2nd international round-robin test on EIS measurements of organic coatings, Prog. Org. Coat. 180 (2023) 107565.

[23] H. Zhang, L. Hao, J. Wang, S. Zhang, C. Zhang, W. Ke, EIS evaluation on the degradation behavior of rust-preventive oil coating exposure to NaCl electrolyte, Electrochim. Acta 492 (2024) 144359.

[24] C. Liu, Q. Bi, A. Matthews, EIS comparison on corrosion performance of PVD TiN and CrN coated mild steel in 0.5 N NaCl aqueous solution, Corros. Sci. 43 (10) (2001) 1953–1961.

[25] L. Ya-long, D. Tian-shun, L. Guo-lu, W. Hai-dou, F. Bin-Guo, Z. Xiao-dong, Microstructure evolution and properties of NiCrBSi thick coating remelted by gas tungsten arc, Surf. Coat. Technol. 349 (2018) 260–271, https://doi.org/10.1016/j.surfcoat.2018.05.064.

[26] T. Gómez-del Río, M.A. Garrido, J.E. Fernández, M. Cadenas, J. Rodríguez, Influence of the deposition techniques on the mechanical properties and microstructure of NiCrBSi coatings, J. Mater. Process. Technol. 204 (1) (2008) 304–312, https://doi.org/10.1016/j.jmatprotec.2007.11.042.

[27] C. Gu, C.D. Ridgeway, M.P. Moodispaw, A.A. Luo, Multi-component numerical simulation and experimental study of dendritic growth during solidification processing, J. Mater. Process. Technol. 286 (2020) 116829, https://doi.org/10.1016/j.jmatprotec.2020.116829.

[28] H. Li, Y. Xie, H. Wang, Z. Qian, P. Cao, W. Zhang, Facile formation of a thin chromium carbide coating on diamond particles via quaternary molten salt, J. Alloys Compd. 928 (2022) 167142, https://doi.org/10.1016/j.jallcom.2022.167142.

[29] F.W.C. Farias, J. da Cruz Payão Filho, L.M.B. de Azevedo, Microstructural and mechanical characterization of the transition zone of 9 % Ni steel cladded with Ni-based superalloy 625 by GTAW-HW, Metals (Basel) 8 (12) (2018) 1007.

[30] S. Sudhagar, M. Sakthivel, P. Ganeshkumar, Monitoring of friction stir welding based on vision system coupled with Machine learning algorithm, Measurement 144 (2019) 135–143.

[31] Y. Bai, H. Zheng, H. Zhang, Y. Shao, H. Zhang, J. Zhu, A melting pre-bonding method for fabrication of mechanical-robust superhydrophobic powder coatings, Prog. Org. Coat. 182 (2023) 107680, https://doi.org/10.1016/j.porgcoat.2023.107680.

[32] K. Hu, X. Jiang, H. Yu, D. Sun, Solidification and corrosion mechanisms: A novel metallurgical bonding Ti-6Al-4V coating on mild steel, Surf. Coat. Technol. 476 (2024) 130258, https://doi.org/10.1016/j.surfcoat.2023.130258.

[33] K. Deenadayalan, V. Murali, A. Elayaperumal, S. Arulvel, Effective role of short time furnace heat treatment and laser treatment on the residual stress and mechanical properties of NiCrBSi–WC weldments produced using plasma transferred arc welding process, J. Mater. Res. Technol. 15 (2021) 3492–3513, https://doi.org/10.1016/j.jmrt.2021.09.113.

[34] L.-Y. Chen, et al., Phase interaction induced texture in a plasma sprayed-remelted NiCrBSi coating during solidification: An electron backscatter diffraction study, Surf. Coat. Technol. 358 (2019) 467–480, https://doi.org/10.1016/j.surfcoat.2018.11.019.

[35] C. Shi, J. Lei, S. Zhou, X. Dai, L.-C. Zhang, Microstructure and mechanical properties of carbon fibers strengthened Ni-based coatings by laser cladding: The effect of carbon fiber contents, J. Alloys Compd. 744 (2018) 146–155, https://doi.org/10.1016/j.jallcom.2018.02.063.

[36] I. Hemmati, J. Rao, V. Ocelík, Jt. De Hosson, Electron microscopy characterization of Ni-Cr-B-Si-C laser deposited coatings, Microsc. Microanal. 19 (1) (2013) 120–131.

[37] S. Dong, B. Song, H. Liao, C. Coddet, Deposition of NiCrBSi coatings by atmospheric plasma spraying and dry-ice blasting: Microstructure and wear resistance, in: 6th Rencontres Int. Proj. Therm. 268, 2015, pp. 36–45, https://doi.org/10.1016/j.surfcoat.2014.09.025.

[38] N. Siredey-Schwaller, J. Hamel-Akré, L. Peltier, A. Hazotte, P. Bocher, Solidification sequence of Ni-Si-Cr∼ 3wt % B brazing alloys, Weld. World 61 (2017) 1253–1265.

[39] G. Cacciamani, A. Dinsdale, M. Palumbo, A. Pasturel, The Fe–Ni system: Thermodynamic modelling assisted by atomistic calculations, Intermetallics 18 (6) (2010) 1148–1162, https://doi.org/10.1016/j.intermet.2010.02.026.

[40] K. Barmak, et al., Critical events, entropy, and the grain boundary character distribution, Phys. Rev. B 83 (13) (2011) 134117.

[41] W. Feng, S. Yang, Y. Yan, Dependence of grain boundary character distribution on the initial grain size of 304 austenitic stainless steel, Philos. Mag. 97 (13) (2017) 1057–1070.

[42] B. Wu, et al., Effects of synchronized magnetic arc oscillation on microstructure, texture, grain boundary and mechanical properties of wire arc additively manufactured Ti6Al4V alloy, Addit. Manuf. 54 (2022) 102723, https://doi.org/10.1016/j.addma.2022.102723.

[43] X. Guo, et al., Cooperative enhancement of strength and corrosion resistance through architecture of nanotwins and low angle grain boundary in Ni20Cr alloy, Corros. Sci. 227 (2024) 111759, https://doi.org/10.1016/j.corsci.2023.111759.

[44] V. Randle, Role of grain boundary plane in grain boundary engineering, Mater. Sci. Technol. 26 (7) (2010) 774–780.

[45] J.W. Key, J. Kacher, Establishing first order correlations between pitting corrosion initiation and local microstructure in AA5083 using automated image analysis, Mater. Charact. 178 (2021) 111237, https://doi.org/10.1016/j.matchar.2021.111237.

[46] P. Xiang, J. Cao, Q. Long, S. Wang, J. Wu, Z. Abbas, Tribological properties of PTFE/PI-PAI composite coatings filled by GO/ZrO2 on the surfaces of different micro-textures, Colloids Surf. Physicochem. Eng. Asp. 686 (2024) 133412, https://doi.org/10.1016/j.colsurfa.2024.133412.

[47] Y. Xie, K. Shibata, T. Mizoguchi, A brute-force code searching for cell of non-identical displacement for CSL grain boundaries and interfaces, Comput. Phys. Commun. 273 (2022) 108260, https://doi.org/10.1016/j.cpc.2021.108260.

[48] V. Randle, Mechanism of twinning-induced grain boundary engineering in low stacking-fault energy materials, Acta Mater 47 (15) (1999) 4187–4196, https://doi.org/10.1016/S1359-6454(99)00277-3.

[49] V. Randle, Twinning-related grain boundary engineering, Acta Mater 52 (14) (2004) 4067–4081, https://doi.org/10.1016/j.actamat.2004.05.031.

[50] Z. Shi, Y. Meng, Effects of indentation depth and grain size on scratching behavior of nanograin FCC Fe polycrystalline substrate, Tribol. Int. 193 (2024) 109464, https://doi.org/10.1016/j.triboint.2024.109464.

[51] X. Zhao, Z. Yue, G. Wang, Z. Li, C. Soyarslan, Role of GNDs in bending strength gain of multilayer deposition generated heterostructured bulk aluminum, Mater. Des. (2022) 110769.

[52] P. Snopiński, A.N.S. Appiah, O. Hilšer, M. Kotoul, Investigation of Microstructure and Mechanical Properties of SLM-Fabricated AlSi10Mg Alloy Post-Processed Using Equal Channel Angular Pressing (ECAP), Materials (Basel) 15 (22) (2022) 7940.

[53] A. Eghlimi, M. Shamanian, M. Eskandarian, A. Zabolian, J.A. Szpunar, Characterization of microstructure and texture across dissimilar super duplex/austenitic stainless steel weldment joint by super duplex filler metal, Mater. Charact. 106 (2015) 27–35, https://doi.org/10.1016/j.matchar.2015.05.017.

[54] H. Wang, R. Sun, M. Zhang, B. Gou, J. Mo, Impact-sliding behavior of Ni-based coating prepared on tunnel boring machine disc cutter material produced using a plasma transferred arc welding process, Spec. Issue Surf. Coat. Technol. Celebr. Pioneer. Res. Career Profr. Allan Matthews Field Plasma-Based Surf. Eng. 442 (2022) 128186, https://doi.org/10.1016/j.surfcoat.2022.128186.

[55] H.-N. Xuan, et al., Temperature profile, microstructural evolution, and wear resistance of plasma-sprayed NiCrBSi coatings under different powers in a vertical remelting way, Mater. Chem. Phys. 292 (2022) 126773, https://doi.org/10.1016/j.matchemphys.2022.126773.

[56] F.A. Najar, S. Rathee, M. Srivastava, A. Yadav, Tribological and Corrosion Behaviour of Al-Mg-CeO2 Metal Matrix Surface Composites, Tribol. Int. (2024) 109508, https://doi.org/10.1016/j.triboint.2024.109508.

[57] J. Lei, Y. Hu, Z. Liu, G.J. Cheng, K. Zhao, Defects mediated corrosion in graphene coating layer, ACS Appl. Mater. Interfaces 9 (13) (2017) 11902–11908.

[58] S. Julie, M.K. Dash, N.P. Wasekar, C. David, M. Kamruddin, Effect of annealing and irradiation on the evolution of texture and grain boundary interface in electrodeposited nanocrystalline nickel of varying grain sizes, Surf. Coat. Technol. 426 (2021) 127770, https://doi.org/10.1016/j.surfcoat.2021.127770.

[59] H. Fu, W. Wang, X. Chen, G. Pia, J. Li, Grain boundary design based on fractal theory to improve intergranular corrosion resistance of TWIP steels, Mater. Des. 185 (2020) 108253.

[60] Q. He, et al., Effect of annealing on microstructure and corrosion behavior of interstitial free steel, Materials (Basel) 15 (1) (2021) 24.

[61] J. Fu, K. Cui, F. Li, J. Wang, Y. Wu, Texture and anisotropic mechanical properties of ferritic stainless steel stabilized with Ti and Nb, Mater. Charact. 159 (2020) 110027, https://doi.org/10.1016/j.matchar.2019.110027.

[62] M. Mukherjee, S. Saha, T.K. Pal, P. Kanjilal, Influence of modes of metal transfer on grain structure and direction of grain growth in low nickel austenitic stainless steel weld metals, Mater. Charact. 102 (2015) 9–18, https://doi.org/10.1016/j.matchar.2015.02.006.

[63] M. Gustafsson, M. Thuvander, E.-L. Bergqvist, E. Keehan, L. Karlsson, Effect of welding procedure on texture and strength of nickel based weld metal, Sci. Technol. Weld. Join. 12 (6) (2007) 549–555.

[64] O. Muránsky, I. Karatchevtseva, A.E. Danon, R. Holmes, P. Huai, Z. Zhang, Impact of dislocations and dislocation substructures on molten salt corrosion of alloys under plasticity-imparting conditions, Corros. Sci. 176 (2020) 108915, https://doi.org/10.1016/j.corsci.2020.108915.

[65] M. Maric, et al., The effect of cold-rolling on the microstructure and corrosion behaviour of 316L alloy in FLiNaK molten salt, Corros. Sci. 142 (2018) 133–144, https://doi.org/10.1016/j.corsci.2018.07.006.

[66] X. Chen, M. Gussev, M. Balonis, M. Bauchy, G. Sant, Emergence of micro-galvanic corrosion in plastically deformed austenitic stainless steels, Mater. Des. 203 (2021) 109614, https://doi.org/10.1016/j.matdes.2021.109614.

[67] S. Li, et al., Enhancing tribological properties of 18CrNiMo7-6 through grain refinement incorporating Al2O3 particles, Tribol. Int. 190 (2023) 109045, https://doi.org/10.1016/j.triboint.2023.109045.

[68] Z. Li, X. Zhao, Z. Tan, C. Kong, H. Yu, Microstructure and texture evolution of pure nickel during cryorolling and subsequent annealing, J. Mater. Res. Technol. 24 (2023) 6739–6752, https://doi.org/10.1016/j.jmrt.2023.04.173.

[69] Z. Cai, S. Wang, Y. Zhou, J. Dong, C. Yu, L. Ma, The synergistic effect of grain refinement and precipitation strengthening on mechanical properties and dry sliding wear behavior of medium manganese steels, Tribol. Int. 179 (2023) 108158, https://doi.org/10.1016/j.triboint.2022.108158.

[70] M. Varenberg, Adjusting for running-in: Extension of the Archard wear equation, Tribol. Lett. 70 (2) (2022) 59.

[71] C. Tsallis, Possible generalization of Boltzmann-Gibbs statistics, J. Stat. Phys. 52 (1988) 479–487.

[72] C. Tsallis, Nonadditive entropy and nonextensive statistical mechanics-an overview after 20 years, Braz. J. Phys. 39 (2009) 337–356.

[73] G. Kaniadakis, M. Lissia, A. Scarfone, Deformed logarithms and entropies, Phys. Stat. Mech. Its Appl. 340 (1–3) (2004) 41–49.

[74] A. Rajagopal, Dynamic linear response theory for a nonextensive system based on the Tsallis prescription, Phys. Rev. Lett. 76 (19) (1996) 3469.

[75] A. Rajagopal, Von Neumann and Tsallis entropies associated with the Gentile interpolative quantum statistics, Phys. Lett. A 214 (3–4) (1996) 127–130.

[76] C. Zhang, C. Wang, Y. Yang, G. Yang, A nanoscaled thermodynamic approach in nucleation of CVD diamond on nondiamond surfaces, J. Phys. Chem. B 108 (8) (2004) 2589–2593.

[77] C. Wang, Y. Yang, Q. Liu, G. Yang, Nucleation thermodynamics of cubic boron nitride upon high-pressure and high-temperature supercritical fluid system in nanoscale, J. Phys. Chem. B 108 (2) (2004) 728–731.

[78] C.-X. Wang, Y.-H. Yang, G.-W. Yang, Nanothermodynamic analysis of the low-threshold-pressure-synthesized cubic boron nitride in supercritical-fluid systems, Appl. Phys. Lett. 84 (16) (2004) 3034–3036.

[79] C. Wang, Y. Yang, N. Xu, G. Yang, Thermodynamics of diamond nucleation on the nanoscale, J. Am. Chem. Soc. 126 (36) (2004) 11303–11306.